Discovery of 34 low-mass comoving systems using NOIRLab Source Catalog DR2

Frank Kiwy [1], Jacqueline K. Faherty [2], Aaron Meisner [3], Adam C. Schneider [4,5]
J. Davy Kirkpatrick [6], Marc J. Kuchner [7], Adam J. Burgasser [8], Sarah Casewell [9], Rocio Kiman [10]
Emily Calamari [11], Christian Aganze [12], Chih-Chun Hsu [12], Arttu Sainio [1], Vinod Thakur,[1] and
The Backyard Worlds: Planet 9 Collaboration

[1]*Backyard Worlds: Planet 9*

[2]*Department of Astrophysics, American Museum of Natural History, Central Park West at 79th Street, NY 10024, USA*

[3]*NSF's National Optical-Infrared Astronomy Research Laboratory, 950 N. Cherry Ave., Tucson, AZ 85719, USA*

[4]*United States Naval Observatory, Flagstaff Station, 10391 West Naval Observatory Rd., Flagstaff, AZ 86005, USA*

[5]*Department of Physics and Astronomy, George Mason University, MS3F3, 4400 University Drive, Fairfax, VA 22030, USA*

[6]*IPAC, Mail Code 100-22, Caltech, 1200 E. California Blvd., Pasadena, CA 91125, USA*

[7]*NASA Goddard Space Flight Center, Exoplanets and Stellar Astrophysics Laboratory, Code 667, Greenbelt, MD 20771, USA*

[8]*Center for Astrophysics and Space Science, University of California, San Diego, La Jolla, CA 92093, USA*

[9]*School of Physics and Astronomy, University of Leicester, University Road, Leicester, LE1 7RH, UK*

[10]*Kavli Institute for Theoretical Physics, University of California, Santa Barbara, CA 93106, USA*

[11]*Department of Physics, Barnard College, Columbia University, New York, NY 10027, USA*

[12]*Department of Physics, University of California, San Diego, La Jolla, CA 92093*

ABSTRACT

We present the discovery of 34 comoving systems containing an ultra-cool dwarf found by means of the NOIRLab Source Catalog (NSC) DR2. NSC's angular resolution of $\sim 1''$ allows for the detection of small separation binaries with significant proper motions. We used the catalog's accurate proper motion measurements to identify the companions by cross-matching a previously compiled list of brown dwarf candidates with NSC DR2. The comoving pairs consist of either a very low-mass star and an ultra-cool companion, or a white dwarf and an ultra-cool companion. The estimated spectral types of the primaries are in the K and M dwarf regimes, those of the secondaries in the M, L and T dwarf regimes. We calculated angular separations between ~ 2 and $\sim 56''$, parallactic distances between ~ 43 and ~ 261 pc and projected physical separations between ~ 169 and ~ 8487 AU. The lowest measured total proper motion is 97 mas yr^{-1}, the highest 314 mas yr^{-1}. Tangential velocities range from ~ 23 to ~ 187 km s^{-1}. We also determined comoving probabilities, estimated mass ratios and calculated binding energies for each system. We found no indication of possible binarity for any component of the 34 systems in the published literature. The discovered systems can contribute to the further study of the formation and evolution of low-mass systems as well as to the characterization of cool substellar objects.

Keywords: Binary stars — Multiple stars — Low-mass stars — Brown dwarfs — White dwarf stars

1. INTRODUCTION

Binary and multiple stellar systems have long been used to study the formation and fundamental properties of stars. With the first discovery of brown dwarf binary systems (Martín et al. 1998; Basri & Martín 1999; Martín et al. 1999), these investigations have been extended into the substellar regime. Physical properties of individual brown dwarfs (e.g. mass, metallicity or surface gravity) are difficult to determine due to the absence of main sequence hydrogen burning, causing them to cool and fade over time. For brown dwarfs in multiple systems, however, physical properties, age and composition can be inferred from their stellar companions. Further, the binary fraction, mass ratio distribution and separation of brown dwarf companion systems can provide constraints on star formation and dynamical evolution (Goodwin & Whitworth 2007).

One valuable type of benchmark systems are those with a wide binary composed of resolved companions, the primary being a main sequence star and the secondary being an L or T dwarf. Because it is very difficult to determine properties such as metallicity and age

of L and T dwarfs, these properties can be inferred from the primary since comoving systems are assumed to have formed at the same time, from the same material and developed in the same environment. However, benchmark systems involving L or T dwarf companions are more difficult to find than systems composed of earlier type companions, because often either the primary is saturated or the secondary remains undetected. Moreover, the binary fraction seems to decrease from early to late primary spectral types (Kraus & Hillenbrand 2012). While the binary fraction for solar type stars ranges within 50-60% (Duquennoy & Mayor 1991; Raghavan et al. 2010), it decreases to 30-40% for M stars (Fischer & Marcy 1992; Delfosse et al. 2004; Janson et al. 2014; Winters et al. 2019). For field brown dwarfs, the resolved binary fraction for very low-mass systems is around 10-20% (Close et al. 2003; Burgasser et al. 2006; Gelino et al. 2011; Huélamo et al. 2015; Fontanive et al. 2018).

Identifying comoving companions has become easier through the use of large, multi-epoch surveys such as the Wide-field Infrared Survey Explorer (Wright et al. 2010), the *Gaia* Mission (*Gaia* Collaboration et al. 2016), or the DESI Legacy Imaging Surveys (Dey et al. 2019). Resulting catalogs like CatWISE2020 (Marocco et al. 2021), *Gaia* DR2 (*Gaia* Collaboration et al. 2018), *Gaia* EDR3 (*Gaia* Collaboration et al. 2021) or NSC DR2 (Nidever et al. 2021) are excellent resources for finding late-type moving objects and their potential companions by using the provided proper motions. Two objects sufficiently close to each other on the sky and having comparable proper motions can provide a basis for inferring a common origin.

This paper is outlined as follows. In Section 2, we briefly describe the NSC and its key elements relevant to this work. In Section 3, we present our search method, and in Section 4, we characterize the discovered systems. We discuss some of the systems in more detail in Section 5.

2. NOIRLAB SOURCE CATALOG DR2

NSC DR2 (Nidever et al. 2021) is based on public image data from the NOIRLab Astro Data Archive. These images come from telescopes in both hemispheres (CTIO–4m+DECam, KPNO–4m+Mosaic3 and Bok–2.3m+90Prime) and cover $\sim 35,000$ square degrees of the sky. A significant part of the images were obtained by the Dark Energy Survey (Abbott et al. 2018) and the DESI Legacy Imaging Surveys (Dey et al. 2019). NSC DR2 includes more than 3.9 billion single objects with over 68 billion individual source measurements. It has depths of $\sim$ 23rd magnitude in most broadband filters

(u, g, r, i, z, Y and VR), accurate proper motions and an astrometric accuracy of $\sim$ 7 mas.

NSC provides proper motion measurements that push much fainter at optical wavelengths than *Gaia* DR2 or EDR3. At g-band, NSC is $\sim$ 2.5 magnitudes deeper than *Gaia* and allows proper motion searches for distant stars with high tangential velocities over a volume $\sim$ 25 times larger than *Gaia*. NSC can also measure motions for white dwarfs much fainter than those detected by *Gaia*, expanding the census of white dwarfs in the solar neighborhood. NSC's accurate proper motions enable the discovery of ultra-cool white dwarf binaries where metallicity and radial velocity can be derived from a main sequence companion (Lam et al. 2020).

Due to its excellent red-optical sensitivity and sky coverage, NSC provides many new possibilities to search for ultra-cool stars and brown dwarfs in the solar neighborhood. CatWISE2020 (Marocco et al. 2021) represents one of the best infrared proper motion catalogs currently available. However, at its faint end, CatWISE motions are only significant above $\sim 150 - 200$ mas yr^{-1}, unlike NSC, which can measure motions many times smaller at high significance. NSC's Y-band depth (23.4 mag) and angular resolution ($\sim 1''$) allow for motion searches of late-type objects not possible with WISE. This enables queries for pairs of faint objects with consistent proper motions to find closely spaced low-mass companion systems.

3. SEARCH METHOD

In a first step, we searched for previously missed L and T dwarfs in the NOIRLab Source Catalog using proper motion and photometry. We used the z, i and Y magnitudes along with the relations described in Carnero Rosell et al. (2019) to determine the color cut for our initial selection. We required all objects having at least one detection in each of those three bands. The adopted color cut ($1.4 < (i-z)_{NSC} < 3.5$ and $0.4 < (z-Y)_{NSC} < 1.5$) should restrict the search to L and T dwarfs. However, it cannot be excluded that some late M dwarfs are within the selected objects. Note that both color constraints had to be satisfied for this selection. No quality cuts were applied to the photometry to avoid eliminating more distant late-type/faint objects with less accurate photometry. Candidates having proper motions below 100 mas yr^{-1} have been discarded from the selection to provide proper motions significant enough to be visually confirmed by blinking images of different epochs. We avoided the galactic plane ($|b| > 15°$) to further reduce the number of sources with spurious proper motions. We required a high Star/Galaxy classifier of at least 0.7 to ensure that the search only returns objects

with a point-like morphology. The Star/Galaxy classifier is a NSC catalog column which provides information on an object's probability of being either a galaxy or a star, based on its morphology. Selected objects had to have a time baseline of at least six months between the first and last observation. By applying these criteria, we obtained a total of 2896 candidate ultracool dwarfs, mostly in the L and T regimes.

In a second step, we examined a $100''$ radius around all 2896 objects using the NSC by comparing the proper motion components of each object to the proper motion components of the objects found in the defined radius. We applied a proper motion matching tolerance of 20 mas yr^{-1} to find potential companions either of earlier or later type. Note that we exclusively used NSC DR2 proper motions for this purpose. As in the first step, we excluded objects having a Star/Galaxy classifier below 0.7 and a time baseline of less than six months. To further reduce the number of false positives, each identified companion was cross-matched with *Gaia* EDR3 to discard objects with a parallax below 2 mas. This resulted in 46 pairs with similar proper motions.

Among those 46 potential companions, we found four false positives (no object visible in WISE or DECaLS imagery), three likely false positives with significant differences in their proper motion components, and thirteen known pairs, one of which (NSC J2322−6151) is referenced in Smart et al. (2019) and Calissendorff et al. (2019), the other twelve find mention in the SUPER-WIDE catalog (Hartman & Lépine 2020). The known pairs, which are listed in Table 1 (Rediscovered systems), are not further described in this paper.

We repeated both steps described above using a slightly different color cut than in the first selection ($i_{NSC} > 99$ and $0.4 < (z - Y)_{NSC} < 1.5$). The goal of this second selection was to target specifically substellar sources and not more distant warmer stars. Since late-type brown dwarfs emit more radiation in the near infrared, an i-band dropout is a strong signature for detecting a cold compact source. We therefore dropped the i−z color but used the same constraints for the z−Y color than in the first selection. We also required selected objects explicitly to have no i-band photometry by adding a corresponding constraint ($i > 99$) to exclude any objects found in the first selection. After applying the first step of our search method, we obtained a total of 2520 objects. Step two resulted in three additional systems, #2, #21 and #24, having secondaries with estimated spectral types of T5, T3 and T0, respectively.

Each object has been visually inspected to determine whether its proper motion components are consistent with those of its comoving companion by blinking images of different epochs. For this, we used `AstroToolBox` (Kiwy 2022), which is a Java tool set with a graphical user interface allowing us to blink either unWISE coadds (Meisner et al. 2017, 2018) of epochs 2010 and 2014-2020, or DECaLS cutouts (Dey et al. 2019) from DR5, DR7, DR8 and DR9. DECaLS cutouts have a resolution $10\times$ higher than unWISE coadds ($0.27''$/pixel vs. $2.75''$/pixel), making it possible to identify the components of binary systems down to an angular separation of $\sim 1''$. All objects have been carefully checked against at least one background star, showing no visible motion, to eliminate false positives produced by misaligned images.

To assess the effect of the photometric uncertainties on the selection, we calculated the mean photometric error associated with the $(i-z)_{NSC}$ and $(z-Y)_{NSC}$ colors of the secondaries in our sample, which is 0.035 mag for both of these colors (Table 8). The used color cut ($1.4 < i-z < 3.5$ and $0.4 < z-Y < 1.5$) was determined by the means of the Carnero Rosell et al. (2019) relations with the following color values for the given spectral types: {L0, T9} = {($i-z = 1.48, z-Y = 0.43$), ($i-z = 3.39, z-Y = 1.5$)}. Note that the Carnero Rosell relations do not give uncertainties on their color values. When we subtract the mean photometric errors from the color values for spectral type L0, we obtain the following values: $i-z = 1.48 - 0.035 = 1.445$ and $z-Y = 0.43 - 0.035 = 0.395$. While the value for the i−z color is still above the lower limit of our color cut, that for the z−Y color is 0.005 mag below the limit. Given this small color value difference, we conclude that it has minimal, if any, effect on the selection. As for the upper limits of the used color cut, the photometric errors do not affect the selection since our sample does not contain objects with estimated spectral types later than T5. This corresponds to the color values $i-z = 3.25$ and $z-Y = 1.02$ from the Carnero Rosell relations, which both are well below the upper bounds of the employed color cut ($i-z = 3.5, z-Y = 1.5$), and stay well below even if we add the mean photometric uncertainties ($i-z = 3.25 + 0.035 = 3.285$ and $z-Y = 1.02 + 0.035 = 1.055$).

Aside from the 29 new systems discovered through the method described above, an additional five new systems (#3, #11, #16, #25 and #27) were recovered serendipitously when visually checking a list of objects from a previous NSC DR2 search focused on high proper motion ultra-cool dwarf candidates. The color and proper motion cuts used in that search were somewhat different from those applied in step one of this work. In each of these cases, the companion could be identified through `AstroToolBox`'s image blinker. For those five systems, either the primary or the secondary did not

satisfy all the constraints defined in the search method of this work.

At the same time these searches were on-going, several members of the Backyard Worlds: Planet 9 citizen science project (Kuchner et al. 2017) were searching for similar cold compact objects via the Zooniverse portal or via a research scientist guided side project. Arttu Sainio recovered system #21, Vinod Thakur recovered systems #13, #20, and Sam Goodman recovered systems #1 and #35. Details on those searches and additional discoveries by the larger Backyard Worlds team will be reported in a forthcoming paper.

We identified a total of 34 new candidate binary systems, most of which are located in the DES footprint (Abbott et al. 2021). The general properties of these systems are given in Table 1 (Newly discovered systems) with additional astrometry from NSC DR2 in Table 2 and relevant photometry in Table 7. Histograms showing the distribution of distances, angular and physical separations, total proper motions and tangential velocities can be found in Figure 2.

4. CHARACTERIZING SYSTEMS

4.1. *Spectral Type Estimates*

We evaluated the photometric quality of our sample by calculating the weighted mean of all photometric errors in all bands of the employed photometric systems. Since the secondaries are generally fainter and often blended by the primaries, we calculated the weighted mean separately and found that it is 0.015 mag for the primaries and 0.078 mag for the secondaries (Table 8). We deduce that the overall photometric quality of our sample is good and even excellent for most of the primaries but degrades for the secondaries (with regard to the primaries).

We plotted different types of color-magnitude diagrams (CMDs), using *Gaia* EDR3 G-band versus G – G_{RP} color, Pan-STARRS DR2 z-band versus z – y color, NSC DR2 z-band versus z – Y color, and VISTA VHS DR5 J-band versus J – Ks color (Figure 3). For the *Gaia* CMD, we plotted the primaries on a comparative sample composed of late K and M dwarfs (K8-M9) and DA white dwarfs extracted from the SIMBAD database (Wenger et al. 2000). For the Pan-STARRS, NSC and VISTA VHS CMDs, we used as a comparative sample the M dwarfs from Best et al. (2018) and the L & T dwarfs from Best et al. (2020). The M dwarfs were cross-matched with *Gaia* EDR3 to obtain the parallaxes to calculate the absolute magnitudes. M, L and T dwarfs were cross-matched with NSC and VISTA VHS to get the corresponding photometry. A radius of 2″ was used for both cross-matches. We split the comparative sample into early and late-type M, L and T dwarfs and used a different color for each of these categories. We always plotted all the systems having the corresponding photometry on each of those CMDs.

According to our color-magnitude diagrams, we found 31 systems composed of a main sequence star and an ultra-cool companion, and 3 systems composed of a white dwarf and an ultra-cool companion. The estimated spectral types of the main-sequence stars are in the late-K and M dwarf regimes, those of the ultra-cool companions in the late-M, L and early-T dwarf regimes. Our search resulted in 1 K+L, 11 M+M, 16 M+L, 3 M+T, 1 WD+M and 2 WD+L systems. More accurate spectral type estimates can be found in Table 1.

The spectral type estimates were obtained from `AstroToolBox`'s Photometric Classifier, which uses the available photometry along with the relations from Kiman et al. (2019), Carnero Rosell et al. (2019), Best et al. (2018) and Mamajek (2021) to establish a spectral type classification by counting the occurrences of each determined spectral type. Kiman et al. (2019) relates to *Gaia* photometry for spectral types M0 to L7, Carnero Rosell et al. (2019) relates to DES, VHS and AllWISE photometry for spectral types M1 to T9, and Best et al. (2018) relates to Pan-STARRS, 2MASS and WISE photometry for spectral types M0 to T9. The Mamajek (2021) relations are using *Gaia* photometry for spectral types B9-L8, Sloan photometry for spectral types M0-T8, 2MASS photometry for spectral types O9-Y1, and WISE photometry for spectral types B5-K5 and M5-Y4. `AstroToolBox` does not account for photometric uncertainties, but relies on the number of equal spectral type estimates from the various photometric systems and corresponding relations. For each object, we retained the spectral type with the most occurrences. In case there were two or more distinct spectral types with the same number of occurrences, we kept the one whose photometric distance best fits the *Gaia* parallax. When considering the mean photometric error of our sample in each of the used colors (Table 8), we infer a spectral type uncertainty of about one sub-type for the primaries and two sub-types for the secondaries.

4.2. *Spectroscopy*

4.2.1. *Kast Optical Spectrograph*

Optical spectroscopy was obtained for the primary of system #8 (NSC J0153–0015A) using the Kast Double Spectrograph mounted on the Lick 3m Shane Telescope on 2021 Dec 12 (UT). Conditions were cloudy with average seeing of 1″3. Two exposures of 1500 s each were obtained in the red channel using the 600/7500 grating and 1″5-wide slit, providing 6000–9000 Å at an average res-

olution of $\lambda/\Delta\lambda = 1900$. Only one of the exposures was used due to the deteriorating weather conditions. The flux standard Feige 110 was observed at the start of the night for flux calibration, and the G2 V star HD 13043 was observed after NSC J0153–0015A to measure telluric absorption. Data were reduced and analyzed using the `kastredux` package[1] with default settings. The reduced spectrum, shown in Figure 4 (bottom left panel), has an average signal-to-noise of $\approx$25, due to the poor transparency. Nevertheless, we detect an overall red spectral energy distribution and weak molecular features consistent with an early-type M dwarf. We compared this spectrum to M dwarf optical template spectra from Bochanski et al. (2007), finding a best match to the M1 template, which we adopt for the classification of this primary.

4.2.2. *SpeX Infrared Prism Spectroscopy*

We observed the secondary in system #21 using the SpeX spectrograph on NASA's IRTF telescope. The spectrum was taken on the night of 23 October 2021 (UT), under good conditions with minimal cloud coverage, in prism mode using the 0.8″ slit to achieve a resolving power of ∼100 - 500 over the 0.8 - 2.5 μm coverage. We obtained 7 AB nods using 180 s exposures on the target and then acquired the A0 star HD 32855 for telluric correction using 1 s exposures and 10 AB nods. All data were reduced using the `Spextool` package (Cushing et al. 2004) with telluric correction and flux calibration of the A0 stars following the technique described in Vacca et al. (2003). In Figure 4 (top right panel) we compare this spectrum to several T dwarf standards from Burgasser et al. (2004) and find a good agreement with the T3 standard, which confirms our spectral type estimate for this object.

4.3. *Distance Estimates*

Photometric distances were calculated for the secondaries by employing relevant spectro-photometric distance conversions. We used the spectral type estimates from `AstroToolBox` and derived the corresponding absolute magnitudes from Table 4 in Kiman et al. (2019) and Table 6 in Best et al. (2018). For each photometric system, we calculated distances using the bands covered by the above relations and retained the minimum and maximum values of the photometric system with the best match. For a given magnitude, we estimated an average distance difference between a given sub-type (e.g. L5) and its lower and upper neighbors (L4, L6) of ∼ 20% of the sub-type's (L5) photometric distance.

These estimations were done by comparing the distances of the lower and upper neighbors of a given sub-type at different magnitudes and in different bands. Since we assume a spectral type uncertainty of two sub-types for the secondaries, this can lead to distance discrepancies of up to ∼ 40% of the secondary's photometric distance, depending on the quality of the photometry used for the spectral type estimates. A comparison between the parallactic distance of the primaries and the mean photometric distance of the secondaries is presented in Table 3, which also contains the bands used to calculate the minimum and maximum photometric distances as well as the spectral types employed to derive the absolute magnitudes for those calculations. We have illustrated the distance difference between the primaries and the secondaries in Figure 1. Note that for systems #9 and #15, the parallactic distance of the primary is about twice the photometric distance of the secondary, which we discuss further in Section 5.
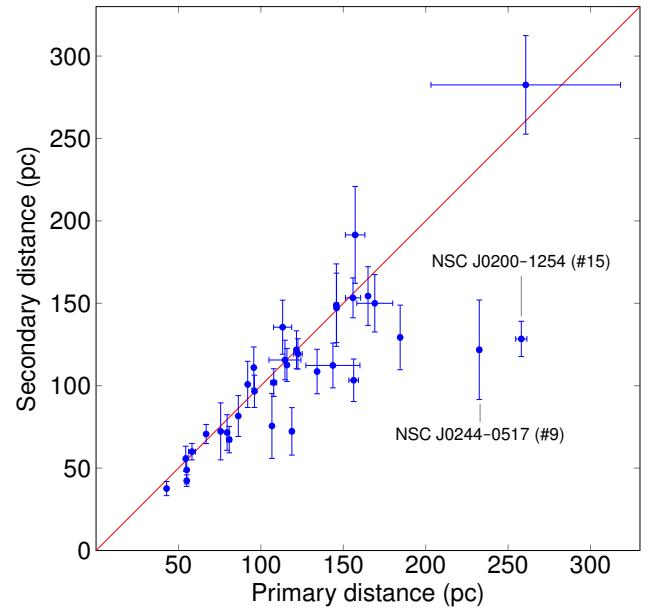
Figure 1. Secondary mean photometric distance versus primary parallactic distance.

4.4. *Chance Alignment*

We determined comoving probabilities using the Co-Mover code from Gagné et al. (2021), which uses the sky position, proper motion, parallax and optionally the heliocentric radial velocity of the host star with their respective errors, and compares these with the observables of the potential companion on the basis of various star models.

We executed the code once without a distance constraint and once with a distance constraint on the sec-

ondaries, since most photometric distances of our secondaries are based on spectral type estimates only. Also, the blending caused by some of the primaries can lead to inaccurate photometry, affecting spectral type and photometric distance estimates.

The resulting comoving probabilities are shown in Table 3. Those without a distance constraint are all $>=$ 99.3% except for system #13, which only has a comoving probability of 73.6%. Those with a distance constraint are $>=$ 99.8% except for three systems (#9, #13 and #15), which all have comoving probabilities significantly lower than 100% (59.8, 87.0 and 4.5% respectively).

We used the sky positions and proper motions with their respective errors from NSC DR2 for the primaries and secondaries. The parallax and associated error of the primaries are from *Gaia* EDR3. The parallax and corresponding error of the secondaries were inferred from their mean photometric distance, based on the spectral type estimates from `AstroToolBox`. As seen previously, a difference of two sub-types corresponds to a distance discrepancy of $\sim 40\%$. To determine how much the comoving probabilities change with a difference of two sub-types, we increased the photometric distance of the secondaries by 40% and re-ran the `CoMover` code. We found that most systems, which already had a high comoving probability, still have a high one after increasing the distance (see Table 3 columns 3 vs. 4).

4.5. *Literature Information*

We searched the literature for any derived physical properties for the primaries and secondaries of the newly discovered systems. All of these properties are from either Stassun et al. (2019) or Gentile Fusillo et al. (2021) and are given in Table 4 along with all other literature references. Fundamental parameters were not available for any of the secondaries in our new systems. However, two of them find mention in Skrzypek et al. (2016), which does not contain physical properties. Some of our primaries are referenced by one or more of the following literary sources: Reylé (2018), Pokorny et al. (2003), Luyten (1995), Eggen (1976a), Eggen (1976b), Salim & Gould (2003), Wroblewski & Torres (1996), Kirkpatrick et al. (2016). None of these works include fundamental parameters.

4.6. *Astrometry*

We calculated distances and tangential velocities for all our systems using the *Gaia* EDR3 astrometry of the primaries (Table 1). Position angles, angular and physical separations were calculated by correcting the position of the primary for proper motion to the epoch of the secondary. NSC DR2 positions and mean ob-

servation epochs were used for this purpose. All separations were calculated using the general case equation $\theta = \cos^{-1} \left[\sin \delta_A \sin \delta_B + \cos \delta_A \cos \delta_B \cos(\alpha_A - \alpha_B) \right]$ to account for systems having larger RA coordinate separations at high declination. In Table 2, we computed the difference in proper motion between the primaries and secondaries, taking into account the errors in μ_α and μ_δ. We also found that there is good agreement between the *Gaia* and NSC proper motions of the primaries (see *Gaia* proper motions in Table 1 versus NSC proper motions in Table 2). Note that none of our secondaries has proper motions in *Gaia*.

4.7. *Mass Ratios and Binding Energies*

To compute total masses, mass ratios and binding energies for each systems (Table 5), we estimated component masses using a combination of literature references and relations described below. Table 4 lists masses for the primary stars. For mass estimates of the secondaries we used either the Mamajek (2021) relation for sources with absolute G magnitude < 17, or we extrapolated from the spectral type to dynamical mass values computed in Dupuy & Liu (2017). In Figure 5, we overplotted our systems with the collection of very low-mass systems compiled in Faherty et al. (2020) as well as the collection of binaries from Faherty et al. (2021). We have omitted any system with a comoving probability $< 98\%$ (#9, #13 and #15). The majority of our sources lie near the locus of field comoving sources as they have estimated total masses $> 0.2 \, \mathrm{M}_\odot$. Three systems (#2, #11 and #14) have estimated total masses $< 0.2 \, \mathrm{M}_\odot$ as they contain low-mass secondaries (T5, L8, L4 respectively) with low-mass host stars ($\sim$ M7). These three systems are at the low end of the binding energy distribution for field companion systems but still well contained within the locus of known sources.

4.8. *Age and Mass Estimates for the White Dwarfs*

We performed age, initial and final mass estimates for the three white dwarf primaries (systems #25, #27 and #33) included in our sample. We used `wdwarfdate`[2] (Kiman et al. in prep.), which is an open source code that estimates ages of white dwarfs in a Bayesian framework. It runs a chain of models to estimate the ages and their uncertainties from an effective temperature and a surface gravity. The code determines the age of the progenitor star, the cooling age of the white dwarf, and the total age. The age of the ultra-cool companion can be inferred directly from the total age of the white dwarf, provided that both formed at the same time. `wdwarfdate`

---

[2] https://github.com/rkiman/wdwarfdate

also estimates the initial mass (that of the progenitor star) and the final mass (that of the white dwarf). The code uses the cooling tracks from (Bédard et al. 2020) to estimate the parameters of the white dwarfs, and MIST stellar evolutionary tracks computed with the Modules for Experiments in Stellar Astrophysics (MESA) (Paxton et al. 2011, 2013, 2015; Dotter 2016; Choi et al. 2016). See also Lu et al. (2021) who used the code to estimate the age of main sequence stars comoving with a white dwarf, to compare with the results of their age-dating method.

Since our three white dwarfs are in Gentile Fusillo et al. (2021), we had the required parameters to run the code using Cummings et al. (2018) initial-to-final mass relation. As we don't know the composition of our white dwarfs (we are only working from the photometry), we ran the code using the derived T_{eff} and log g for DA and DB white dwarfs, provided by Gentile Fusillo. The results are presented in Table 6. The final mass estimates are more or less consistent with those from Gentile Fusillo. Since the white dwarf of system #25 has a very low-mass (0.256 ± 0.159 M$_\odot$), which is outside the range of the initial-to-final mass relation described in Cummings et al. (2018), `wdwarfdate` cannot estimate the main sequence age and mass of the progenitor star. However, the code can estimate the mass and cooling age of the white dwarf using Bédard et al. (2020) cooling tracks.

4.9. Finder Charts

Figure 6 compares color composites from unWISE NEO7 with DESI Legacy Imaging Surveys (LS) DR9. The purpose of these images is to show the difference between low-resolution surveys such as WISE (FWHM $\sim 6''$ for the short channels, Wright et al. 2010) compared to high-resolution surveys such as DES (FWHM $\sim 1''$, Abbott et al. 2018) or VISTA VHS (FWHM $\sim 0.9''$, Sutherland et al. 2015) when it comes to identifying binary systems that are less widely separated, in which case WISE would only show one blended source rather than the resolved pair.
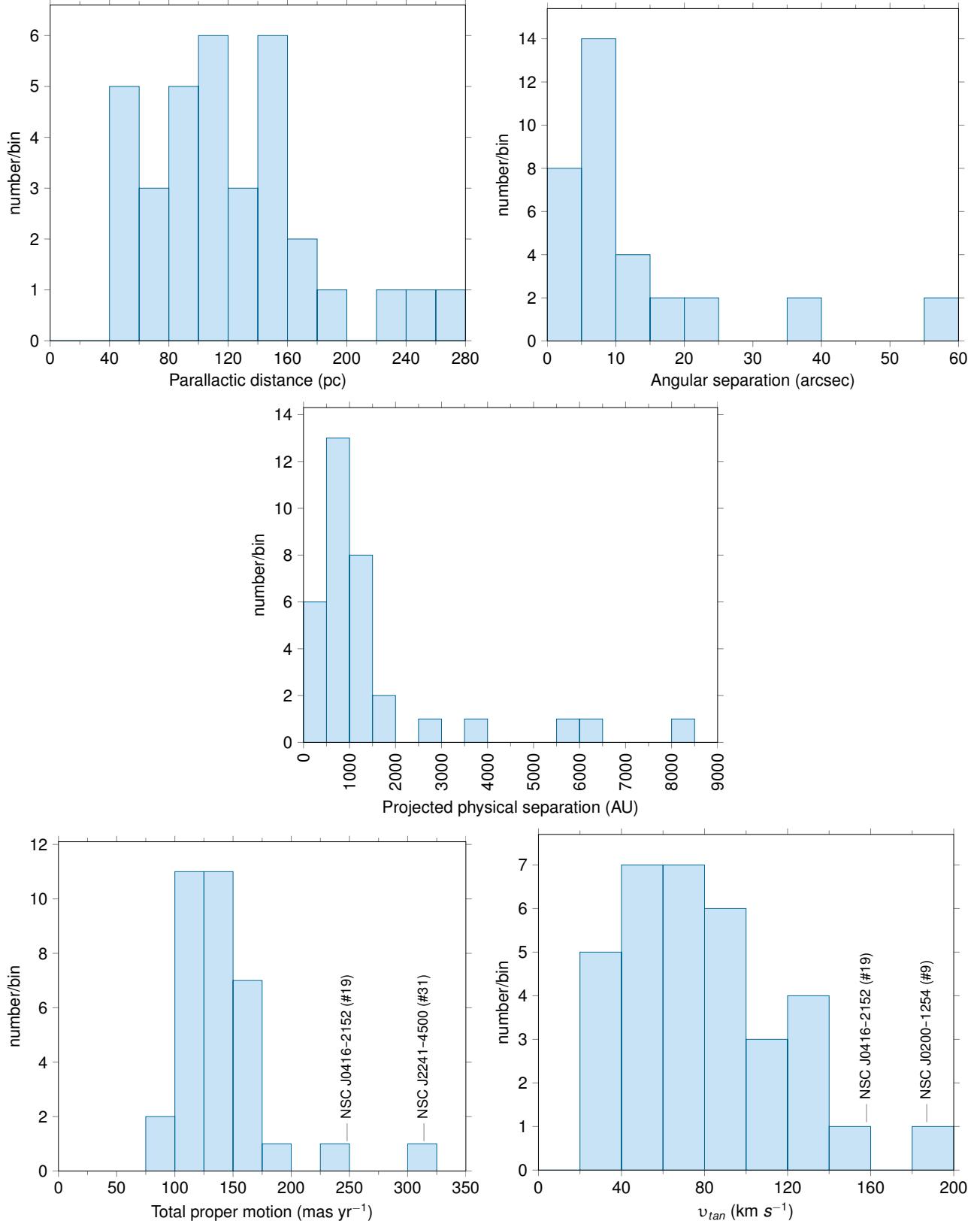
Figure 2. Distributions of parallactic distance, angular separation, projected physical separation, total proper motion and $v_{\tan}$ from Tables 1 and 2.
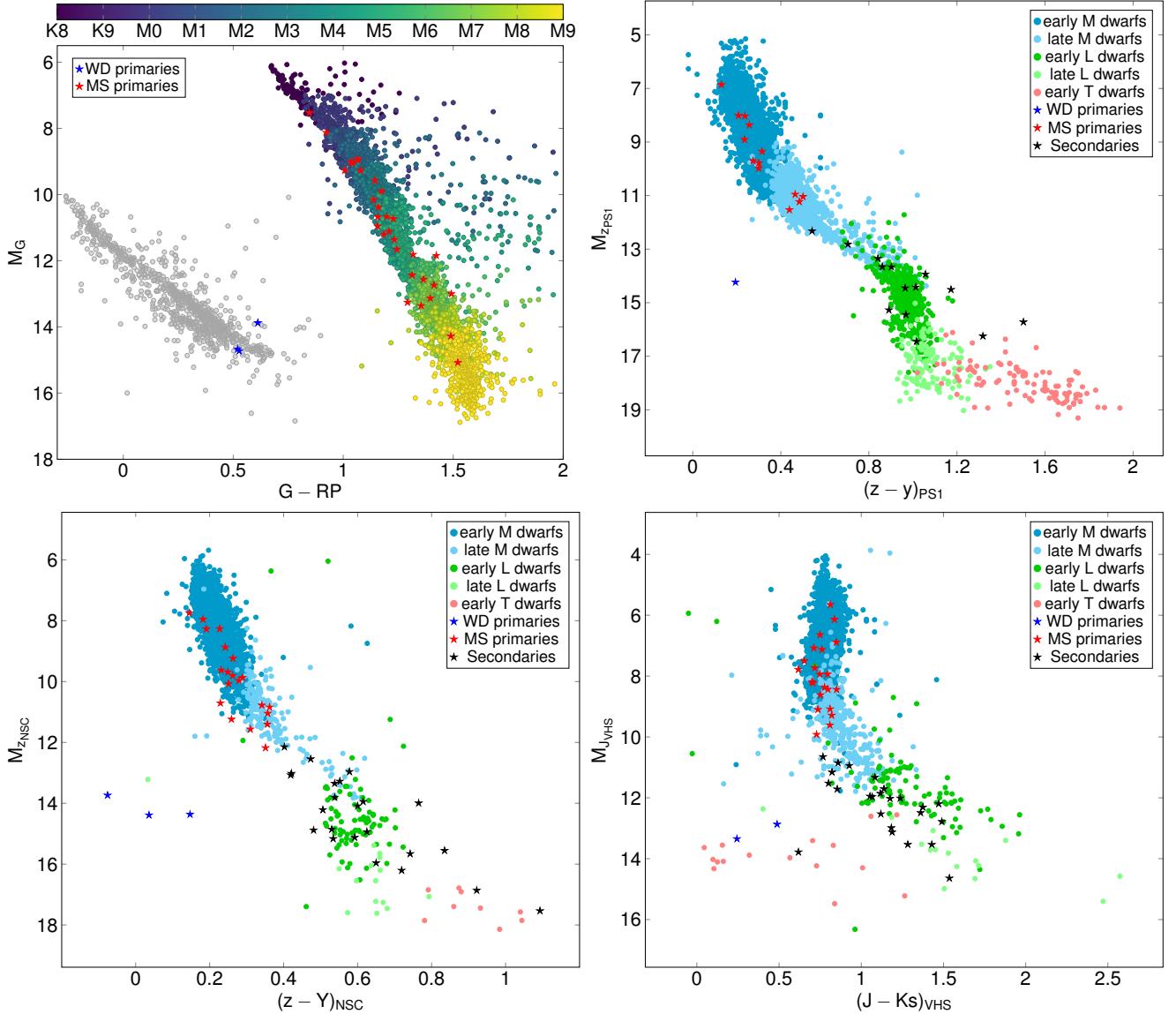
Figure 3. Top left panel: *Gaia* CMD of the primaries. Top right panel: Pan-STARRS CMD; Bottom left panel: NSC CMD; Bottom right panel: VHS CMD. Five-pointed star symbols: the blue stars represent the white dwarf (WD) primaries, the red stars correspond to the main sequence (MS) primaries, and the black stars refer to the secondaries. We used the parallax of the primaries to calculate the absolute magnitude of the secondaries.
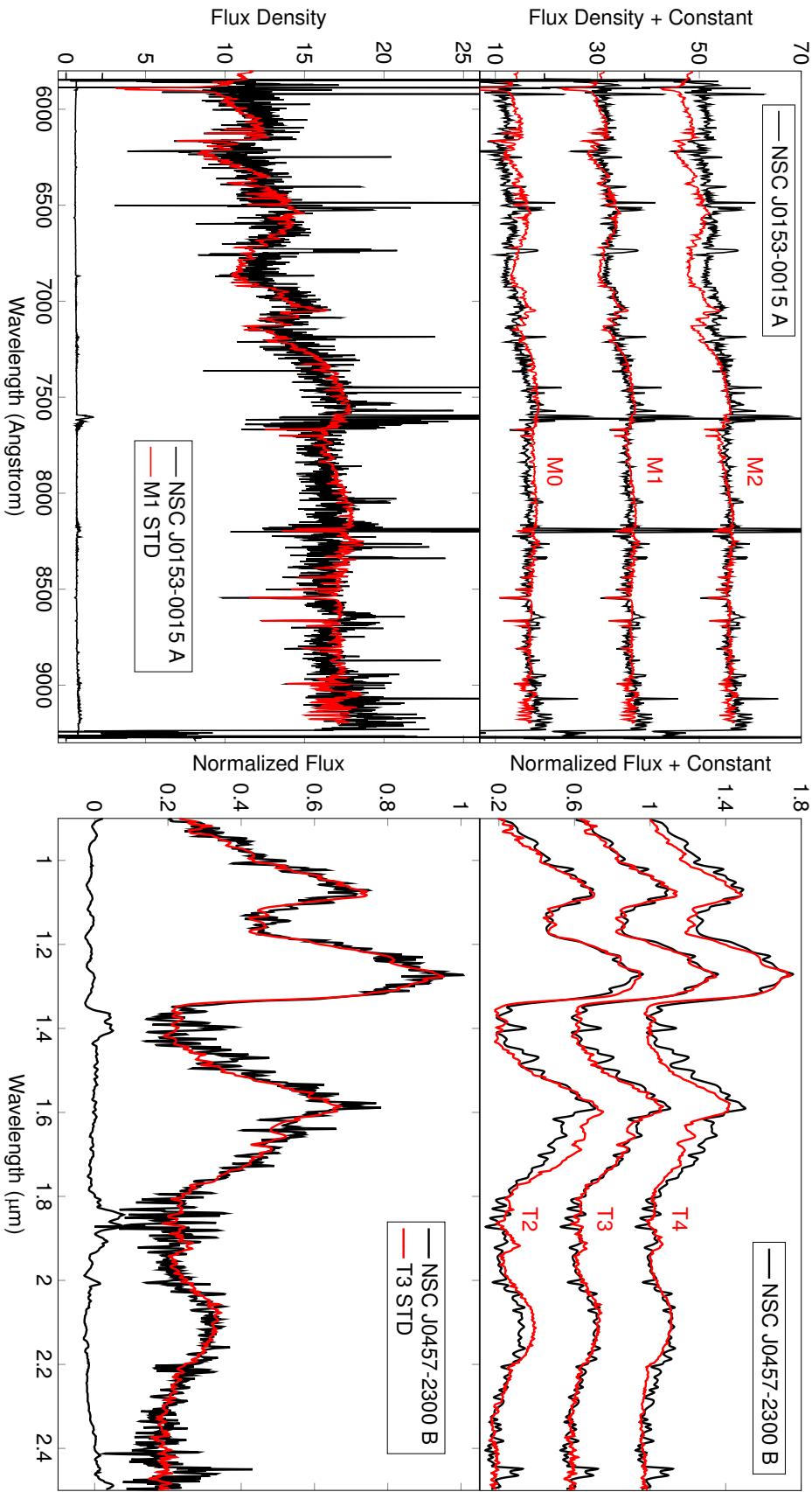
Figure 4. Top left panel: Optical spectrum of NSC J015340.10-001550.34 A (primary of system #8) compared to three M dwarf standards from Bochanski et al. (2007). The spectrum of our primary (smoothed for a better comparison) fits best with the M1 standard. Bottom left panel: Unsmoothed version of the same spectrum with the M1 standard overplotted. Top right panel: Near-infrared spectrum of NSC J045724.25-230012.74 B (secondary of system #21) compared to three T dwarf standards from Burgasser et al. (2004). The spectrum of our secondary (smoothed for a better comparison) fits best with the T3 standard. Bottom right panel: Unsmoothed version of the same spectrum with the T3 standard overplotted.
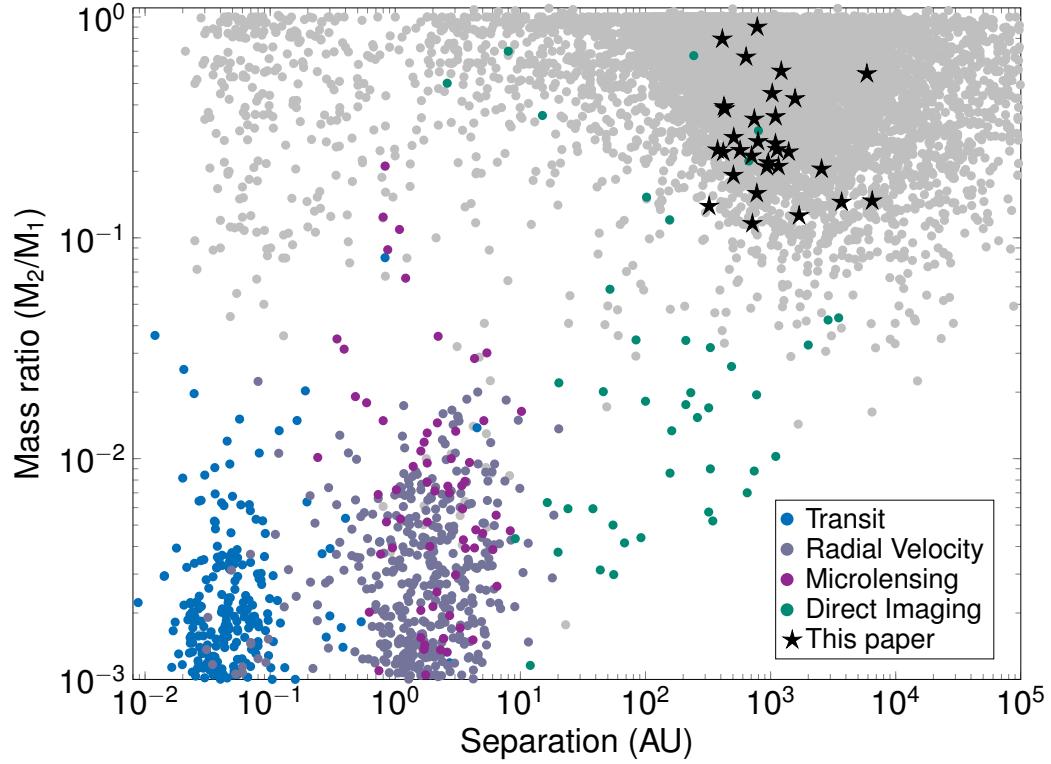
Figure 5. Mass ratio (secondary/primary) versus projected separation for literature sources taken from Faherty et al. 2020 and Faherty et al. 2021 (various color coded filled circles) and companions from this paper (black five-pointed stars). We have color coded the exoplanet detections (as defined by the Exoplanet Archive) by the detection method of the source.
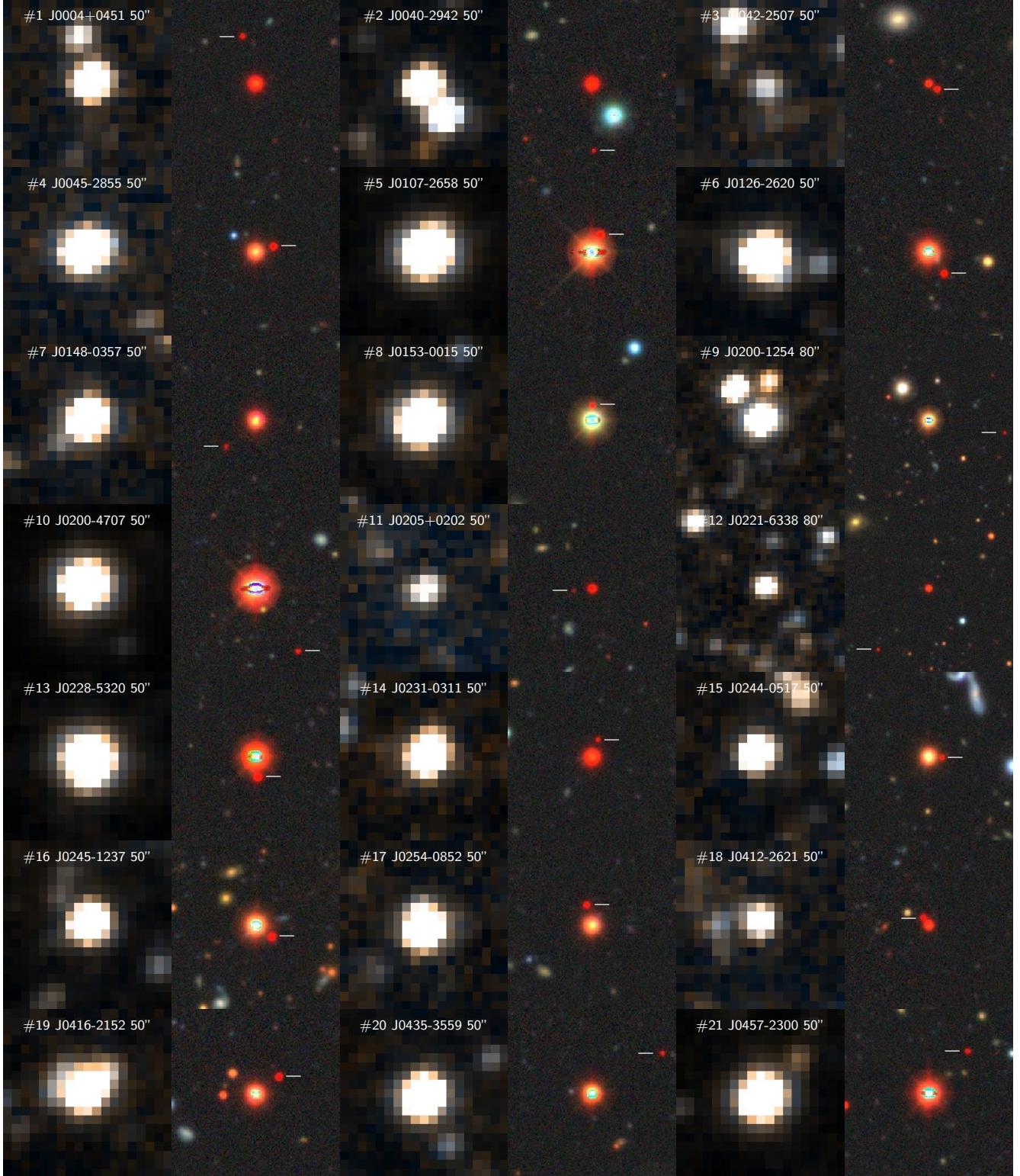
Figure 6. unWISE NEO7 versus LS DR9 images (north up, east to the left). We used VISTA VHS DR6 images for systems #27 and #28 since there is no corresponding LS DR9 imagery. The primaries are in the center of the images, the secondaries were marked by a white dash. White lettering indicates the system number and name followed by the size of the field of view ($50'' \times 50''$, $80'' \times 80''$ or $120'' \times 120''$, depending on the angular separation of the system components).

#22 J0504-4822 50"
#23 J0505-4750 50"
#24 J0523-5655 50"
#25 J0532-5124 50"
#26 J1239-0054 50"
#27 J1305-2247 50"
#28 J1320-4012 120"
#29 J2023-4844 50"
#30 J2208-5510 50"
#31 J2241-4500 50"
#32 J2327-5247 120"
#33 J2333-6347 50"
#34 J2344+0031 50"
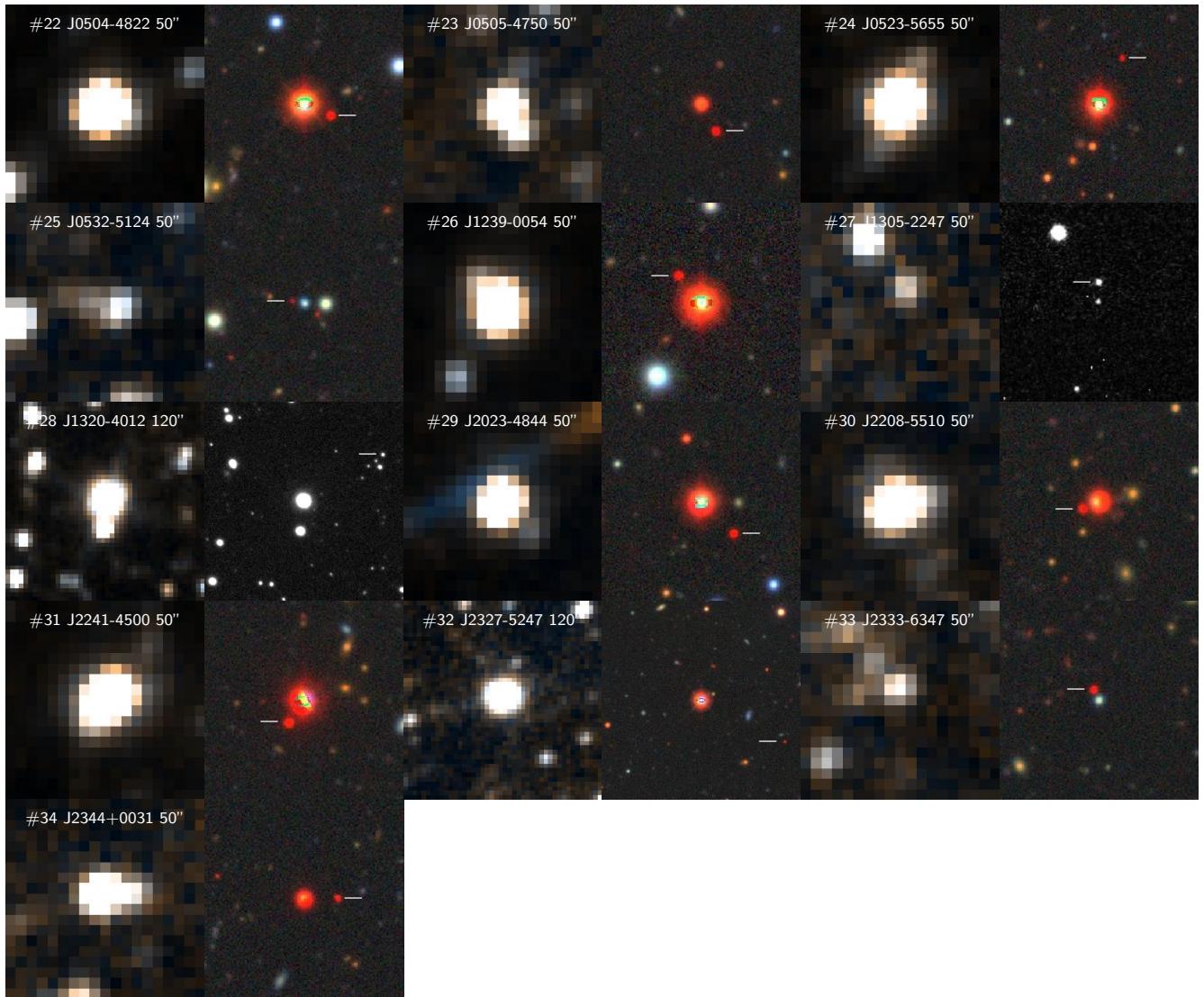
Figure 6 (Continued)

Table 1. Discovered systems

| Sys. #	System name	Short name	ϖ (mas)	μ_α (mas yr^{-1})	μ_δ (mas yr^{-1})	Dist.[a] (pc)	v_{tan}[b] (km s^{-1})	Sep.[c] ($''$)	Sep.[d] (AU)	Pos.[e] (deg)	Sys.[f] type	Ref.[g]
	NEWLY DISCOVERED SYSTEMS											
1	NSC J000456.31+045117.22 AB	NSC J0004+0451	9.2747±0.1585	100.538±0.206	10.524±0.146	107.821±1.843	51.663±0.889	14.548	1568.531	15.4	M6+L2	⋯
2	NSC J004058.68-294212.37 AB	NSC J0040-2942	18.1726±0.1292	84.313±0.128	-124.955±0.143	55.028±0.391	39.318±0.282	19.906	1095.379	181.2	M7+T5	⋯
3	NSC J004239.82-250714.01 AB	NSC J0042-2507	3.8355±0.8464	109.022±0.936	-17.709±0.846	260.725±57.535	136.499±30.144	3.000	782.216	237.1	M6+M6	⋯
4	NSC J004509.91-285557.20 AB	NSC J0045-2855	6.8596±0.0544	93.307±0.055	-24.9±0.061	145.78±1.156	66.732±0.531	5.447	794.110	286.4	M4+M9	⋯
5	NSC J010717.67-265848.32 AB	NSC J0107-2658	11.5915±0.0202	115.191±0.021	-119.037±0.027	86.27±0.15	67.736±0.118	5.846	504.352	333.8	M1+M8	⋯
6	NSC J012629.63-262023.18 AB	NSC J0126-2620	6.8549±0.0307	101.256±0.04	-51.201±0.027	145.882±0.653	78.459±0.352	7.921	1155.583	215.7	M3+M8	⋯
7	NSC J014827.71-035716.63 AB	NSC J0148-0357	8.4201±0.0628	52.933±0.081	-175.686±0.042	118.764±0.886	103.292±0.771	11.752	1395.736	131.3	M4+L4	⋯
8	NSC J015340.10-001550.34 AB	NSC J0153-0015	5.4188±0.0236	83.398±0.029	-105.841±0.02	184.544±0.804	117.871±0.514	4.206	776.150	359.0	M1+M8	⋯
9	NSC J020029.71-125451.00 AB	NSC J0200-1254	4.3019±0.0211	146.841±0.021	-84.873±0.018	232.455±1.14	186.876±0.917	36.509	8486.735	260.8	K7+L9	⋯
10	NSC J020048.45-470755.84 AB	NSC J0200-4707	13.2326±0.0145	107.904±0.013	-4.801±0.014	75.571±0.083	38.69±0.043	22.380	1691.254	213.5	M2+L4	⋯
11	NSC J020541.24+020249.66 AB	NSC J0205+0202	8.7286±0.736	-81.262±0.898	-73.003±0.67	114.566±9.66	59.321±5.021	5.561	637.127	95.9	M7+L8	⋯
12	NSC J022132.42-633807.41 AB	NSC J0221-6338	6.4144±0.1885	101.832±0.25	43.48±0.237	155.9±4.581	81.823±2.411	37.757	5886.303	140.4	M6+L1	⋯
13	NSC J022821.48-532004.36 AB	NSC J0228-5320	10.8681±0.0441	127.645±0.045	27.171±0.049	92.012±0.373	56.918±0.232	5.962	548.533	185.2	M3+M8	⋯
14	NSC J023113.30-031147.09 AB	NSC J0231-0311	12.3836±0.2079	24.676±0.236	-128.072±0.195	80.752±1.356	49.923±0.841	5.246	423.614	341.3	M7+L4	⋯
15	NSC J024433.27-051711.10 AB	NSC J0244-0517	3.8755±0.0509	27.951±0.051	-104.003±0.049	258.033±3.389	131.717±1.731	3.905	1007.524	265.6	M1+L0	⋯
16	NSC J024507.25-123726.57 AB	NSC J0245-1237	6.0612±0.0295	34.715±0.033	-141.047±0.034	164.983±0.803	113.593±0.554	5.808	958.154	234.1	M2+M7	⋯
17	NSC J025450.03-085252.25 AB	NSC J0254-0852	8.2213±0.0638	115.448±0.078	-48.647±0.064	121.635±0.944	72.23±0.562	6.095	741.364	14.9	M3+L0	⋯
18	NSC J041239.68-262105.02 AB	NSC J0412-2621	6.3603±0.24	-10.497±0.189	-164.793±0.27	157.225±5.933	123.06±4.648	2.617	411.436	36.3	M6+M8	⋯
19	NSC J041641.96-215248.86 AB	NSC J0416-2152	7.4598±0.0326	117.348±0.027	-219.012±0.032	134.052±0.586	157.878±0.69	8.411	1127.526	306.3	M3+M9	⋯
20	NSC J043503.99-355911.42 AB	NSC J0435-3559	9.3695±0.0287	-8.94±0.027	-96.481±0.034	106.729±0.327	49.018±0.151	23.948	2555.901	299.7	M4+L5	⋯
21	NSC J045724.25-230012.74 AB	NSC J0457-2300	18.187±0.0217	-128.657±0.015	7.236±0.02	54.984±0.066	33.584±0.04	16.970	933.096	317.3	M4+T3	⋯
22	NSC J050456.74-482240.01 AB	NSC J0504-4822	12.574±0.0199	-3.188±0.023	132.932±0.029	79.529±0.126	50.126±0.08	7.175	570.648	248.1	M3+L0	⋯
23	NSC J050506.28-475035.19 AB	NSC J0505-4750	6.3997±0.1196	70.225±0.131	88.813±0.184	156.256±2.92	83.858±1.572	7.787	1216.806	208.4	M6+M9	⋯
24	NSC J052307.20-565522.36 AB	NSC J0523-5655	18.3926±0.0234	-28.942±0.029	156.764±0.029	54.37±0.069	41.083±0.053	12.995	706.547	333.2	M5+T0	⋯
25	NSC J053232.31-512450.75 AB	NSC J0532-5124	5.9143±0.3818	102.804±0.432	138.888±0.479	169.081±10.915	138.487±8.948	3.003	507.731	80.4	WD+L3	⋯
26	NSC J123900.73-005433.72 AB	NSC J1239-0054	23.3826±0.0281	-103.965±0.036	-47.8±0.032	42.767±0.051	23.196±0.029	8.817	377.062	39.8	M4+L4	⋯
27	NSC J130527.23-224728.44 AB	NSC J1305-2247	6.9608±0.7951	-140.208±1.111	2.719±0.754	143.661±16.41	95.493±10.934	4.983	715.907	358.1	WD+L3	⋯
28	NSC J132017.47-401258.27 AB	NSC J1320-4012	14.9605±0.0182	-17.48±0.016	-117.831±0.016	66.843±0.081	37.742±0.046	55.312	3697.213	300.0	M1+L1	⋯
29	NSC J202349.63-484435.01 AB	NSC J2023-4844	10.4053±0.0331	13.143±0.032	-132.182±0.028	96.105±0.306	60.511±0.193	11.382	1093.871	225.4	M4+L0	⋯
30	NSC J220852.71-551054.25 AB	NSC J2208-5510	10.4478±0.0612	-136.283±0.061	5±0.055	95.714±0.561	61.871±0.363	4.498	430.541	113.1	M5+M9	⋯
31	NSC J224101.90-450026.44 AB	NSC J2241-4500	17.1738±0.6061	273.035±0.404	-154.157±0.509	58.228±2.055	86.54±3.057	7.183	418.277	144.5	M5+L2	⋯
32	NSC J232703.65-524727.94 AB	NSC J2327-5247	8.6324±0.0161	108.844±0.013	-32.352±0.016	115.842±0.216	62.349±0.117	56.005	6487.802	243.5	M1+L1	⋯
33	NSC J233302.51-634721.39 AB	NSC J2333-6347	8.8339±0.4268	48.71±0.376	-162.431±0.422	113.2±5.469	90.99±4.402	2.851	322.740	26.5	WD+M9	⋯
34	NSC J234443.91+003112.41 AB	NSC J2344+0031	8.1622±0.175	-92.89±0.188	-103.067±0.127	122.516±2.627	80.575±1.73	8.414	1030.796	270.9	M6+L2	⋯
	REDISCOVERED SYSTEMS											
⋯	NSC J002111.11-424540.39 AB	NSC J0021-4245	37.3319±0.0378	255.184±0.031	-12.475±0.039	26.787±0.027	32.439±0.033	77.840	2085.087	316.9	M6+L0	1
⋯	NSC J003011.68-374049.20 AB	NSC J0030-3740	21.0552±0.0576	-86.91±0.042	-65.42±0.059	47.494±0.13	24.489±0.068	89.057	4229.675	312.3	WD+M9	1
⋯	NSC J003320.53-422726.41 AB	NSC J0033-4227	16.4251±0.0183	320.573±0.015	-46.16±0.014	60.883±0.068	93.466±0.104	29.065	1769.531	125.2	M3+L0	1
⋯	NSC J013609.18-255613.81 AB	NSC J0136-2556	13.7237±0.1623	203.037±0.184	17.952±0.095	72.867±0.862	70.4±0.835	7.074	515.438	34.5	WD+L0	1

Table 1 *continued*

Table 1 *(continued)*

Sys.	System name	Short name	ϖ	μ_α	μ_δ	Dist.[a]	v_{tan}[b]	Sep.[c]	Sep.[d]	Pos.[e]	Sys.[f]	Ref.[g]
#			(mas)	(mas yr^{-1})	(mas yr^{-1})	(pc)	(km s^{-1})	($''$)	(AU)	(deg)	type	
⋯	NSC J014953.56-612919.67 AB	NSC J0149-6129	13.0666±0.0544	3.697±0.06	-161.535±0.063	76.531±0.319	58.613±0.245	12.321	942.972	338.5	WD+L0	1
⋯	NSC J020640.61-222439.29 AB	NSC J0206-2224	7.525±0.0578	88.629±0.049	-61.198±0.045	132.89±1.021	67.843±0.522	9.978	1325.982	336.8	M3+M7	1
⋯	NSC J023508.17-041443.11 AB	NSC J0235-0414	17.7429±0.0284	114.207±0.032	-22.807±0.029	56.36±0.09	31.113±0.051	11.587	653.049	340.0	M4+M9	1
⋯	NSC J044142.59-304256.75 AB	NSC J0441-3042	14.7129±0.0408	63.624±0.038	83.713±0.045	67.968±0.188	33.875±0.095	17.664	1200.582	53.6	M5+M9	1
⋯	NSC J124428.51-011900.40 AB	NSC J1244-0119	12.0087±0.0502	-57.115±0.066	-171.286±0.047	83.273±0.348	71.269±0.299	3.080	256.494	252.4	WD+M9	1
⋯	NSC J203439.06-541247.73 AB	NSC J2034-5412	9.3785±0.0857	3.973±0.078	-105.771±0.083	106.626±0.974	53.495±0.491	30.371	3238.356	212.2	M5+M9	1
⋯	NSC J211810.50-472110.21 AB	NSC J2118-4721	15.117±0.0219	153.639±0.02	-216.018±0.016	66.151±0.096	83.118±0.121	3.333	220.509	176.7	M3+M9	1
⋯	NSC J232028.36-495545.70 AB	NSC J2320-4955	13.1006±0.1154	75.9±0.081	-75.051±0.09	76.332±0.672	38.62±0.342	7.363	562.070	2.7	M7+M8	1
⋯	NSC J232252.60-615112.77 AB	NSC J2322-6151	23.5626±0.0296	78.122±0.028	-78.252±0.033	42.44±0.053	22.244±0.029	16.589	704.027	165.6	M5+L2	2,3

NOTE— The parallaxes and proper motions are from *Gaia* EDR3. The primary of system #8 and the secondary of system #21 have confirmed spectral types of M0 and T3, respectively (see spectra in Figure 4). [a]Distance, derived from the *Gaia* EDR3 parallax of the primary; [b]Tangential velocity, calculated using the *Gaia* EDR3 astrometry of the primary; [c]Angular separation; [d]Projected physical separation, calculated using the *Gaia* EDR3 parallax of the primary; [e]Position angle (east of north) of the secondary with respect to the primary; [f]System type, based on spectral type estimates (A+B); [g]Binary system references: (1) Hartman & Lépine (2020), (2) Smart et al. (2019), (3) Calissendorff et al. (2019)
[c,e]Calculated using NSC DR2 positions, translating the position of the primary to the epoch of the secondary.

Table 2. NSC DR2 astrometry

Sys. #	C.[a]	α (deg)	δ (deg)	Epoch	μ_α (mas yr^{-1})	μ_δ (mas yr^{-1})	$\mu_{\rm tot}$ (mas yr^{-1})	$\Delta\mu_\alpha$[b] (mas yr^{-1})	$\Delta\mu_\delta$[c] (mas yr^{-1})	$\Delta\mu_{\rm tot}$[d] (mas yr^{-1})
1	A	1.2346196±0″002078	4.8547833±0″002548	2017-02-17	101.586±2.081	16.224±2.243	102.873±2.085			
	B	1.2356978±0″008701	4.8586783±0″008999	2017-01-31	103.442±10.176	8.665±10.271	103.804±10.177	1.856±10.387	7.559±10.513	7.784±10.506
2	A	10.2445114±0″002146	-29.703435±0″002093	2016-09-23	85.588±1.684	-127.509±1.637	153.57±1.652			
	B	10.2443636±0″015625	-29.7089511±0″015601	2016-05-22	76.615±11.596	-137.72±11.576	157.596±11.581	8.973±11.718	10.211±11.691	13.593±11.703
3	A	10.6659165±0″002078	-25.1205574±0″002254	2017-06-23	110.017±1.081	-18.631±1.168	111.583±1.084			
	B	10.6651479±0″002717	-25.1210108±0″002906	2017-08-07	114.399±1.451	-16.276±1.542	115.551±1.453	4.382±1.809	2.355±1.934	4.975±1.838
4	A	11.2912826±0″002091	-28.9325546±0″002165	2016-10-10	91.114±1.456	-24.391±1.525	94.322±1.461			
	B	11.2896207±0″002027	-28.9321265±0″002127	2016-08-29	98.791±1.421	-25.35±1.474	101.992±1.424	7.677±2.034	0.959±2.121	7.737±2.036
5	A	16.8236365±0″010278	-26.9800885±0″008563	2017-02-24	120.909±13.555	-114.787±11.718	166.718±12.717			
	B	16.822841±0″003846	-26.978638±0″003594	2017-05-15	123.797±3.129	-132.236±2.945	181.141±3.032	2.888±13.911	17.449±12.082	17.686±12.135
6	A	21.6234552±0″003409	-26.3397711±0″003143	2015-08-16	94.787±4.24	-53.296±3.25	108.743±4.024			
	B	21.6220425±0″004235	-26.341568±0″00456	2016-04-26	104.433±2.991	-39.322±3.367	111.591±3.04	9.646±5.189	13.974±4.68	16.98±4.85
7	A	27.1154771±0″002914	-3.9546199±0″002943	2016-02-23	49.302±1.912	-171.409±2.122	178.358±2.107			
	B	27.1179324±0″023287	-3.9567589±0″023424	2015-11-05	68.828±16.381	-168.594±16.504	182.102±16.486	19.526±16.492	2.815±16.64	19.728±16.495
8	A	28.4171021±0″004829	-0.2639823±0″006201	2015-02-22	85.484±2.781	-109.777±4.129	139.135±3.679			
	B	28.4171034±0″004138	-0.2628419±0″004276	2016-01-19	85.823±2.704	-110.007±2.7	139.525±2.702	0.339±3.879	0.23±4.933	0.41±4.24
9	A	30.1238025±0″004582	-12.9141655±0″004964	2015-10-30	146.547±4.654	-85.844±4.933	169.839±4.727			
	B	30.1135648±0″017378	-12.9158077±0″017444	2016-08-11	163.476±11.532	-85.838±11.596	184.642±11.546	16.929±12.436	0.006±12.602	16.929±12.436
10	A	30.2018838±0″006962	-47.1321787±0″005139	2015-03-28	108.767±3.213	-5.923±2.803	108.928±3.212			
	B	30.1968786±0″012833	-47.1373651±0″01282	2016-01-17	109.414±7.503	-7.568±7.513	109.675±7.503	0.647±8.162	1.645±8.019	1.768±8.038
11	A	31.421821±0″003174	2.0471276±0″003597	2016-02-05	-79.908±1.652	-72.908±1.83	108.171±1.735			
	B	31.4233605±0″048468	2.0469716±0″048787	2016-01-06	-79.81±27.969	-79.694±28.054	112.786±28.011	0.098±28.018	6.786±28.114	6.787±28.114
12	A	35.3850943±0″002373	-63.635391±0″002409	2016-05-01	99.186±1.589	40.524±1.59	107.145±1.589			
	B	35.4001583±0″011979	-63.6434698±0″012019	2016-05-15	94.643±7.404	57.983±7.437	110.992±7.413	4.543±7.573	17.459±7.605	18.04±7.603
13	A	37.0895103±0″005066	-53.3345431±0″004095	2015-08-01	128.523±2.28	25.6±2.016	131.048±2.27			
	B	37.0892954±0″003524	-53.3361878±0″003471	2016-03-18	135.364±1.736	44.364±1.681	142.449±1.731	6.841±2.866	18.764±2.625	19.972±2.654
14	A	37.8054288±0″00155	-3.1964142±0″00168	2014-10-19	27.345±0.764	-126.129±0.875	129.059±0.87			
	B	37.8049613±0″019263	-3.195033±0″019493	2014-10-12	23.43±8.058	-122.34±8.252	124.563±8.245	3.915±8.094	3.789±8.298	5.448±8.193
15	A	41.1386057±0″002152	-5.2864157±0″002432	2015-12-06	28.081±1.252	-103.368±1.425	107.114±1.414			
	B	41.1375166±0″009645	-5.2864883±0″009866	2015-07-16	33.115±5.409	-95.38±5.519	100.965±5.507	5.034±5.552	7.988±5.7	9.442±5.658
16	A	41.2802081±0″003752	-12.624046±0″003647	2015-11-18	31.967±3.213	-142.653±3.03	146.191±3.039			
	B	41.2788699±0″003593	-12.6249969±0″003506	2016-01-07	35.216±2.566	-139.192±2.569	143.578±2.569	3.249±4.112	3.461±3.972	4.747±4.038
17	A	43.7084538±0″002476	-8.8811802±0″002285	2016-04-25	117.81±1.636	-47.432±1.418	127±1.607			
	B	43.7088891±0″005807	-8.8795421±0″005976	2016-03-04	122.706±4.318	-50.082±4.482	132.533±4.342	4.896±4.618	2.65±4.701	5.567±4.637
18	A	63.1653339±0″00273	-26.3513948±0″002554	2016-02-12	-11.367±1.854	-171.564±1.774	171.94±1.774			
	B	63.1658141±0″006391	-26.3508035±0″006278	2016-01-03	-21.539±4.404	-165.401±4.288	166.798±4.29	10.172±4.778	6.163±4.64	11.893±4.742
19	A	64.1748361±0″005138	-21.8802396±0″004524	2017-10-14	126.736±6.728	-211.923±5.893	246.928±6.124			
	B	64.1727738±0″004377	-21.8788069±0″004248	2016-12-06	116.722±3.622	-223.551±3.549	252.189±3.565	10.014±7.641	11.628±6.879	15.346±7.213

Table 2 *continued*

Table 2 *(continued)*

Sys.	C.[a]	α	δ	Epoch	μ_α	μ_δ	$\mu_{\rm tot}$	$\Delta\mu_\alpha$[b]	$\Delta\mu_\delta$[c]	$\Delta\mu_{\rm tot}$[d]
#		(deg)	(deg)		(mas yr^{-1})	(mas yr^{-1})	(mas yr^{-1})	(mas yr^{-1})	(mas yr^{-1})	(mas yr^{-1})
20	A	68.7666169±0.″004239	-35.9865056±0.″003406	2015-09-16	-7.196±3.604	-99.253±3.035	99.514±3.038			
	B	68.7594779±0.″018314	-35.9832042±0.″018233	2015-08-06	-19.485±11.443	-100.729±11.386	102.596±11.388	12.289±11.997	1.476±11.784	12.377±11.994
21	A	74.3510223±0.″003104	-23.0035376±0.″003016	2016-12-31	-122.647±2.746	3.851±2.62	122.707±2.746			
	B	74.3475712±0.″009615	-23.0000735±0.″009499	2016-06-02	-117.71±7.21	8.87±7.089	118.044±7.209	4.937±7.715	5.019±7.558	7.04±7.636
22	A	76.2364019±0.″004426	-48.3777799±0.″003606	2015-02-28	-6.873±2.628	131.213±2.716	131.393±2.716			
	B	76.2336175±0.″004861	-48.3785139±0.″004749	2015-06-14	-3.561±3.02	129.436±3.031	129.485±3.031	3.312±4.003	1.777±4.07	3.759±4.018
23	A	76.2761717±0.″002213	-47.8431073±0.″002096	2014-07-23	71.531±1.131	89.929±1.069	114.908±1.093			
	B	76.2746353±0.″003374	-47.8450102±0.″003375	2014-07-09	72.705±1.733	88.922±1.709	114.861±1.719	1.174±2.069	1.007±2.016	1.547±2.047
24	A	80.7800047±0.″003103	-56.9228765±0.″003141	2013-05-15	-20.786±7.213	160.34±7.203	161.682±7.203			
	B	80.7770104±0.″017716	-56.9196198±0.″017769	2014-03-04	-33.032±9.194	160.116±9.229	163.488±9.228	12.246±11.686	0.224±11.707	12.248±11.686
25	A	83.1346048±0.″003653	-51.4140969±0.″003674	2015-02-21	106.814±2.48	137.433±2.484	174.061±2.482			
	B	83.1359277±0.″032688	-51.4139545±0.″032751	2015-03-25	83.45±23.761	158.756±23.832	179.353±23.817	23.364±23.89	21.323±23.961	31.631±23.922
26	A	189.7530615±0.″002337	-0.9093664±0.″002861	2014-03-13	-109.464±1.666	-46.147±2.013	118.794±1.723			
	B	189.7546283±0.″005759	-0.9074848±0.″006148	2014-03-22	-109.687±5.431	-61.573±5.766	125.787±5.513	0.223±5.681	15.426±6.107	15.428±6.107
27	A	196.3634786±0.″00336	-22.7912345±0.″003236	2017-07-09	-137.418±2.968	2.063±3.02	137.433±2.968			
	B	196.3634238±0.″004029	-22.7898509±0.″004017	2017-08-31	-146.575±14.522	-20.231±15.312	147.965±14.537	9.157±14.822	22.294±15.607	24.101±15.496
28	A	200.0728026±0.″00611	-40.2161851±0.″006481	2014-10-18	-14.727±14.628	-129.167±16.618	130.004±16.594			
	B	200.0553734±0.″00314	-40.2084978±0.″00343	2014-05-20	-23.624±2.603	-120.376±2.712	122.672±2.708	8.897±14.858	8.791±16.838	12.508±15.867
29	A	305.9567781±0.″003761	-48.7430579±0.″004199	2016-02-24	14.067±2.045	-135.67±2.292	136.397±2.29			
	B	305.9533633±0.″006408	-48.7452881±0.″006845	2016-06-21	17.981±5.364	-127.904±5.744	129.162±5.737	3.914±5.741	7.766±6.184	8.697±6.097
30	A	332.2196288±0.″002378	-55.1817348±0.″002615	2015-10-03	-136.067±1.465	6.288±1.529	136.212±1.465			
	B	332.2216314±0.″004927	-55.1822256±0.″005096	2015-11-26	-135.249±2.78	9.723±2.781	135.598±2.78	0.818±3.142	3.435±3.174	3.531±3.172
31	A	340.2579184±0.″002945	-45.007344±0.″0032	2015-03-19	270.602±1.938	-150.33±2.114	309.555±1.981			
	B	340.2595948±0.″00365	-45.0089825±0.″003825	2015-07-23	271.007±1.724	-146.575±1.809	308.106±1.744	0.405±2.594	3.755±2.782	3.777±2.78
32	A	351.7652028±0.″005126	-52.7910943±0.″005375	2014-05-10	102.662±3.5	-31.86±3.634	107.492±3.512			
	B	351.7421728±0.″002748	-52.7980402±0.″002734	2014-02-19	109.78±2.967	-30.027±2.953	113.812±2.966	7.118±4.588	1.833±4.683	7.35±4.594
33	A	353.26044±0.″003137	-63.7892751±0.″003392	2015-12-30	43.408±2.348	-161.641±2.417	167.368±2.412			
	B	353.2612406±0.″004994	-63.7885657±0.″005257	2015-12-23	44.617±3.447	-156.7±3.555	162.928±3.547	1.209±4.171	4.941±4.299	5.087±4.292
34	A	356.1829712±0.″00207	0.5201146±0.″002457	2015-06-30	-93.08±1.302	-103.922±1.565	139.512±1.454			
	B	356.180629±0.″008729	0.5201466±0.″009094	2015-09-14	-82.033±5.105	-100.468±5.33	129.704±5.241	11.047±5.268	3.454±5.555	11.574±5.295

Note— [a]Component, where A is the primary and B the secondary of the system; [b]Proper motion difference in right ascension; [c]Proper motion difference in declination; [d]Difference in total proper motion.

Table 3. Comoving probabilities and photometric distances of the secondaries

Sys.	Comoving	Comoving	Comoving	$\Delta\mu_\alpha$	$\Delta\mu_\delta$	Sep.	Parallactic	Mean phot.	$\Delta_{\text{dist.}}$	Min. phot.	Max. phot.	Band min.	Band max.	SpT
#	prob. (%)	prob. (%)	prob. (%)	(mas yr^{-1})	(mas yr^{-1})	(AU)	dist. (pc)	dist. (pc)	(pc)	dist. (pc)	dist. (pc)	phot. dist.	phot. dist.	phot. dist.
(1)	(2)	(3)	(4)	(5)	(6)	(7)	(8)	(9)	(10)	(11)	(12)	(13)	(14)	(15)
1	99.8	100.0	98.5	1.856±10.387	7.559±10.513	1569	107.8±1.8	101.9±8.4	6±8.6	99.5±11	104.3±12.6	z$_{\text{NSC}}$	i$_{\text{NSC}}$	L2
2	99.8	100.0	100.0	8.973±11.718	10.211±11.691	1095	55±0.4	42.4±3.5	12.6±3.5	40.8±4.9	44.1±5	W1$_{\text{CWISE}}$	W2$_{\text{CWISE}}$	T5
3	100.0	100.0	100.0	4.382±1.809	2.355±1.934	782	260.7±57.5	282.5±29.9	21.8±64.8	263.4±36.5	301.7±47.3	y$_{\text{PS1}}$	i$_{\text{PS1}}$	M6
4	100.0	100.0	99.9	7.677±2.034	0.959±2.121	794	145.8±1.2	148.9±25	3.1±25	148.7±34.2	149.2±36.4	RP$_{\text{EDR3}}$	G$_{\text{EDR3}}$	M9
5	99.8	99.9	99.8	2.888±13.911	17.449±12.082	504	86.3±0.2	81.6±12.4	4.7±12.4	80±17.7	83.2±17.3	i$_{\text{DES}}$	z$_{\text{DES}}$	M8
6	99.6	99.8	99.1	9.646±5.189	13.974±4.68	1156	145.9±0.7	147.2±21.1	1.3±21.1	145.1±28.8	149.2±30.9	y$_{\text{PS1}}$	z$_{\text{PS1}}$	M8
7	100.0	98.8	100.0	19.526±16.492	2.815±16.64	1396	118.8±0.9	72.3±14.4	46.4±14.4	71±25.4	73.7±13.5	r$_{\text{DES}}$	i$_{\text{DES}}$	L4
8	100.0	100.0	100.0	0.339±3.879	0.23±4.933	776	184.5±0.8	129.3±19.6	55.2±19.6	125.5±27.8	133.1±27.6	i$_{\text{DES}}$	z$_{\text{DES}}$	M8
9	100.0	59.8	100.0	16.929±12.436	0.006±12.602	8487	232.5±1.1	121.8±30.2	110.6±30.2	119.8±43.1	123.9±42.4	W2$_{\text{CWISE}}$	W1$_{\text{CWISE}}$	L9
10	99.9	100.0	99.9	0.647±8.162	1.645±8.019	1691	75.6±0.1	72.3±17.3	3.2±17.3	60.5±9.2	84.2±33.3	z$_{\text{DES}}$	r$_{\text{DES}}$	L4
11	99.6	99.9	99.1	0.098±28.018	6.786±28.114	637	114.6±9.7	115.6±12	1±15.4	115.4±18.1	115.8±15.7	W2$_{\text{CWISE}}$	W1$_{\text{CWISE}}$	L8
12	99.8	99.9	89.0	4.543±7.573	17.459±7.605	5886	155.9±4.6	153.3±12.1	2.6±12.9	152.6±16.2	153.9±17.9	z$_{\text{NSC}}$	i$_{\text{NSC}}$	L1
13	73.6	87.0	25.7	6.841±2.866	18.764±2.625	549	92±0.4	100.8±14	8.8±14	100±19.3	101.6±20.1	J$_{\text{VHS}}$	K$_{\text{VHS}}$	M8
14	99.9	100.0	100.0	3.915±8.094	3.789±8.298	424	80.8±1.4	67.3±8	13.5±8.2	65.5±10	69±12.6	z$_{\text{DES}}$	i$_{\text{DES}}$	L4
15	100.0	4.5	5.7	5.034±5.552	7.988±5.7	1008	258±3.4	128.4±10.7	129.6±11.3	127.5±15.4	129.3±14.9	i$_{\text{NSC}}$	z$_{\text{NSC}}$	L0
16	100.0	100.0	100.0	3.249±4.112	3.461±3.972	958	165±0.8	154.4±17.8	10.6±17.8	150.8±21.5	157.9±28.4	y$_{\text{PS1}}$	i$_{\text{PS1}}$	M7
17	100.0	100.0	99.7	4.896±4.618	2.65±4.701	741	121.6±0.9	121.8±11.5	0.2±11.5	111.7±14	132±18.2	z$_{\text{SDSS}}$	i$_{\text{SDSS}}$	L0
18	100.0	100.0	100.0	10.172±4.778	6.163±4.64	411	157.2±5.9	191.5±29.4	34.3±29.9	185.2±43.7	197.9±39.2	i$_{\text{PS1}}$	y$_{\text{PS1}}$	M8
19	100.0	100.0	100.0	10.014±7.641	11.628±6.879	1128	134.1±0.6	108.6±13.5	25.4±13.5	106.3±18.2	110.9±20	z$_{\text{PS1}}$	i$_{\text{PS1}}$	M9
20	99.8	99.8	99.9	12.289±11.997	1.476±11.784	2556	106.7±0.3	75.6±19.7	31.2±19.7	59.7±8.1	91.5±38.6	z$_{\text{DES}}$	r$_{\text{DES}}$	L5
21	100.0	100.0	100.0	4.937±7.715	5.019±7.558	933	55±0.1	48.9±8.5	6.1±8.5	47.6±13.4	50.2±10.4	W1$_{\text{UWISE}}$	W2$_{\text{UWISE}}$	T3
22	100.0	100.0	100.0	3.312±4.003	1.777±4.07	571	79.5±0.1	71.6±10.8	8±10.8	64.5±9.3	78.7±19.4	r$_{\text{DES}}$	g$_{\text{DES}}$	L0
23	100.0	100.0	100.0	1.174±2.069	1.007±2.016	1217	156.3±2.9	103.3±12.9	52.9±13.2	92.7±16.7	114±19.7	i$_{\text{NSC}}$	r$_{\text{NSC}}$	M9
24	100.0	100.0	100.0	12.246±11.686	0.224±11.707	707	54.4±0.1	55.7±7.6	1.4±7.6	55±10	56.4±11.4	K$_{\text{VHS}}$	J$_{\text{VHS}}$	T0
25	100.0	100.0	100.0	23.364±23.89	21.323±23.961	508	169.1±10.9	150±17.4	19.1±20.5	145.5±21	154.4±27.7	z$_{\text{NSC}}$	i$_{\text{NSC}}$	L3
26	99.3	100.0	99.9	0.223±5.681	15.426±6.107	377	42.8±0.1	37.6±4.3	5.2±4.3	36.7±6.5	38.5±5.7	i$_{\text{PS1}}$	y$_{\text{PS1}}$	L4
27	99.9	99.9	99.9	9.157±14.822	22.294±15.607	716	143.7±16.4	112.3±13.6	31.4±21.3	111.3±19.6	113.2±18.8	W2$_{\text{CWISE}}$	W1$_{\text{CWISE}}$	L3
28	100.0	100.0	91.6	8.897±14.858	8.791±16.838	3697	66.8±0.1	70.7±5.8	3.9±5.8	68.6±7.2	72.9±9.1	H$_{\text{2MASS}}$	K$_{\text{2MASS}}$	L1
29	100.0	100.0	99.4	3.914±5.741	7.766±6.184	1094	96.1±0.3	96.6±9.8	0.5±9.8	93.9±11.3	99.4±16.1	i$_{\text{DES}}$	r$_{\text{DES}}$	L0
30	100.0	100.0	100.0	0.818±3.142	3.435±3.174	431	95.7±0.6	111±12.5	15.3±12.5	109.6±17.2	112.4±18.1	J$_{\text{VHS}}$	H$_{\text{VHS}}$	M9
31	100.0	100.0	99.9	0.405±2.594	3.755±2.782	418	58.2±2.1	60±5	1.8±5.4	59.8±5.8	60.2±8	J$_{\text{VHS}}$	K$_{\text{VHS}}$	L2
32	100.0	100.0	99.7	7.118±4.588	1.833±4.683	6488	115.8±0.2	112.6±10	3.2±10	95.2±13.1	130±15	r$_{\text{NSC}}$	i$_{\text{NSC}}$	L1
33	100.0	100.0	100.0	1.209±4.171	4.941±4.299	323	113.2±5.5	135.5±16.4	22.3±17.3	134.9±23	136±23.3	W1$_{\text{CWISE}}$	W2$_{\text{CWISE}}$	M9
34	100.0	100.0	98.1	11.047±5.268	3.454±5.555	1031	122.5±2.6	119.3±9.2	3.2±9.5	115.8±11.4	122.8±14.3	J$_{\text{VHS}}$	H$_{\text{VHS}}$	L2

Table 3 *continued*

Table 3 *(continued)*

Sys.	Comoving	Comoving	Comoving	$\Delta\mu_\alpha$	$\Delta\mu_\delta$	Sep.	Parallactic	Mean phot.	$\Delta_{\text{dist.}}$	Min. phot.	Max. phot.	Band min.	Band max.	SpT
#	prob. (%)	prob. (%)	prob. (%)	(mas yr^{-1})	(mas yr^{-1})	(AU)	dist. (pc)	dist. (pc)	(pc)	dist. (pc)	dist. (pc)	phot. dist.	phot. dist.	phot. dist.
(1)	(2)	(3)	(4)	(5)	(6)	(7)	(8)	(9)	(10)	(11)	(12)	(13)	(14)	(15)

Column descriptions:
(1) System number
(2) Comoving probability without a distance constraint on the secondary
(3) Comoving probability with a distance constraint on the secondary
(4) Comoving probability calculated by increasing the secondary's distance by 40% (see Section 4.4)
(5) Proper motion difference in right ascension
(6) Proper motion difference in declination
(7) Projected physical separation
(8) Parallactic distance of the primary
(9) Mean photometric distance of the secondary
(10) Distance difference between the primary (parallactic distance) and secondary (mean photometric distance)
(11) Minimum photometric distance of the secondary for a given photometric system
(12) Maximum photometric distance of the secondary for a given photometric system
(13) Band from which the minimum photometric distance of the secondary was inferred (CWISE and UWISE stand for CatWISE2020 and unWISE DR1, respectively)
(14) Band from which the maximum photometric distance of the secondary was inferred
(15) Spectral type estimate used to derive the absolute magnitude for the photometric distance calculations

Table 4. Fundamental parameters and literature references

Sys. #	Component name	$T_{\rm eff}$ (K)	$\log g$	Mass ($M_\odot$)	Radius ($R_\odot$)	Luminosity ($L_\odot$)	Param. ref.[c]	Other ref.[d]
1	NSC J0004+0451 A	2900±157	5.0627±0.0207	0.17±0.021	0.201±0.007	0.00257±0.00075	1	
1	NSC J0004+0451 B	⋯	⋯	⋯	⋯	⋯		3
2	NSC J0040-2942 A	2823±157	5.2584±0.0648	0.097±0.02	0.121±0.004	0.00084±0.00024	1	4,5
4	NSC J0045-2855 A	3326±157	4.9128±0.0029	0.29±0.021	0.312±0.01	0.01073±0.00273	1	
5	NSC J0107-2658 A	3677±157	4.7644±0.007	0.467±0.02	0.469±0.014	0.03627±0.0084	1	5,6,7,8
6	NSC J0126-2620 A	3435±157	4.7987±0.0058	0.426±0.021	0.431±0.013	0.02327±0.00573	1	
7	NSC J0148-0357 A	3343±158	4.9799±0.0109	0.226±0.02	0.255±0.008	0.00731±0.00187	1	6,9
8	NSC J0153-0015 A	3962±157	4.6746±0.0102	0.565±0.02	0.572±0.017	0.07275±0.01593	1	
9	NSC J0200-1254 A	4205±122	4.6726±⋯	0.66±⋯	0.62±⋯	0.10834±⋯	1	10
10	NSC J0200-4707 A	3577±157	4.7872±0.0058	0.44±0.02	0.444±0.013	0.02903±0.00686	1	
12	NSC J0221-6338 A	3028±166	5.1495±0.0159	0.131±0.022	0.159±0.01	0.00192±0.00068	1	
13	NSC J0228-5320 A	3383±157	4.8175±0.0042	0.403±0.02	0.41±0.012	0.01984±0.00491	1	
14	NSC J0231-0311 A	2900±158	5.1218±0.0274	0.141±0.021	0.171±0.007	0.00187±0.00057	1	
15	NSC J0244-0517 A	3734±157	4.8153±0.0063	0.405±0.022	0.412±0.014	0.0298±0.00707	1	
16	NSC J0245-1237 A	3665±157	4.7833±0.0064	0.444±0.021	0.448±0.014	0.03262±0.00762	1	
17	NSC J0254-0852 A	3410±158	4.9829±0.0112	0.224±0.02	0.253±0.008	0.00777±0.00196	1	
18	NSC J0412-2621 A	3116±165	5.2027±0.0176	0.113±0.022	0.139±0.011	0.00165±0.00061	1	
19	NSC J0416-2152 A	3453±157	4.8909±0.0013	0.315±0.02	0.333±0.01	0.0142±0.00348	1	6,9
20	NSC J0435-3559 A	3406±157	4.9323±0.0062	0.27±0.02	0.294±0.009	0.01049±0.00259	1	
21	NSC J0457-2300 A	3351±157	4.9899±0.0137	0.218±0.02	0.247±0.008	0.00695±0.00174	1	
22	NSC J0504-4822 A	3400±157	4.8947±0.0024	0.31±0.02	0.329±0.01	0.01305±0.00321	1	
23	NSC J0505-4750 A	3085±160	5.1279±0.0257	0.139±0.021	0.168±0.008	0.00232±0.0007	1	
24	NSC J0523-5655 A	3221±157	5.022±0.0185	0.195±0.02	0.225±0.007	0.00492±0.00127	1	11
25	NSC J0532-5124 A	4960±422[a]	7.2249±0.5067[a]	0.256±0.159[a]	⋯	⋯	2	
25	NSC J0532-5124 A	5043±337[b]	7.3208±0.3934[b]	0.283±0.133[b]	⋯	⋯	2	
26	NSC J1239-0054 A	3245±157	4.9843±0.0132	0.222±0.02	0.251±0.008	0.00632±0.00161	1	
26	NSC J1239-0054 B	⋯	⋯	⋯	⋯	⋯		3
27	NSC J1305-2247 A	5373±786[a]	8.076±0.6699[a]	0.63±0.383[a]	⋯	⋯	2	
27	NSC J1305-2247 A	5266±720[b]	8.0029±0.6323[b]	0.571±0.355[b]	⋯	⋯	2	
28	NSC J1320-4012 A	3601±157	4.737±0.0082	0.499±0.02	0.5±0.015	0.03795±0.00892	1	
29	NSC J2023-4844 A	3250±157	4.9134±0.0037	0.29±0.02	0.311±0.01	0.00974±0.0025	1	
30	NSC J2208-5510 A	3055±157	5.0057±0.0142	0.206±0.02	0.236±0.008	0.00438±0.0012	1	
31	NSC J2241-4500 A	3014±157	4.9062±0.0089	0.297±0.026	0.318±0.017	0.00753±0.00241	1	5
32	NSC J2327-5247 A	3620±157	4.7416±0.0081	0.493±0.02	0.495±0.015	0.03794±0.0089	1	
33	NSC J2333-6347 A	5243±318[a]	8.0675±0.2821[a]	0.623±0.175[a]	⋯	⋯	2	
33	NSC J2333-6347 A	5147±285[b]	8.0023±0.2531[b]	0.57±0.143[b]	⋯	⋯	2	
34	NSC J2344+0031 A	2987±160	5.0783±0.0229	0.161±0.02	0.192±0.007	0.00265±0.00077	1	

[a] $T_{\rm eff}$, $\log g$ and mass for DA white dwarfs
[b] $T_{\rm eff}$, $\log g$ and mass for DB white dwarfs
[c] Parameter references: (1) Stassun et al. (2019), (2) Gentile Fusillo et al. (2021)
[d] Other literature references: (3) Skrzypek et al. (2016), (4) Reylé (2018), (5) Pokorny et al. (2003), (6) Luyten (1995), (7) Eggen (1976a), (8) Eggen (1976b), (9) Salim & Gould (2003), (10) Wroblewski & Torres (1996), (11) Kirkpatrick et al. (2016)

Table 5. Total masses, mass ratios and binding energies

Sys.	Sys.	Sep.[a]	M_1[b]	M_2[c]	M_{tot}[d]	M_2/M_1[e]	E_{bin}[f]	SpT$_2$[g]
#	name	(AU)	(M$_\odot$)	(M$_\odot$)	(M$_\odot$)		($\times10^{41}$ erg)	
1	NSC J0004+0451	1568.531	0.170	0.073	0.243	0.427	1.11	L2
2	NSC J0040−2942	1095.379	0.097	0.034	0.131	0.354	0.42	T5
3	NSC J0042−2507	782.216	0.128	0.115	0.243	0.901	2.64	M6
4	NSC J0045−2855	794.110	0.290	0.079	0.369	0.273	4.04	M9
5	NSC J0107−2658	504.352	0.467	0.090	0.557	0.192	11.67	M8
6	NSC J0126−2620	1155.583	0.426	0.090	0.516	0.211	4.65	M8
7	NSC J0148−0357	1395.736	0.226	0.055	0.281	0.245	1.25	L4
8	NSC J0153−0015	776.150	0.565	0.090	0.655	0.159	9.18	M8
9	NSC J0200−1254	8486.735	0.660	0.046	0.706	0.069	0.50	L9
10	NSC J0200−4707	1691.254	0.440	0.055	0.495	0.126	2.00	L4
11	NSC J0205+0202	637.127	0.084	0.055	0.139	0.659	1.02	L8
12	NSC J0221−6338	5886.303	0.131	0.073	0.204	0.554	0.23	L1
13	NSC J0228−5320	548.533	0.403	0.090	0.493	0.223	9.26	M8
14	NSC J0231−0311	423.614	0.141	0.055	0.196	0.393	2.56	L4
15	NSC J0244−0517	1007.524	0.405	0.077	0.482	0.191	4.34	L0
16	NSC J0245−1237	958.154	0.444	0.097	0.541	0.219	6.30	M7
17	NSC J0254−0852	741.364	0.224	0.077	0.301	0.345	3.26	L0
18	NSC J0412−2621	411.436	0.113	0.090	0.203	0.795	3.46	M8
19	NSC J0416−2152	1127.526	0.315	0.079	0.394	0.251	3.09	M9
20	NSC J0435−3559	2555.901	0.270	0.055	0.325	0.205	0.81	L5
21	NSC J0457−2300	933.096	0.218	0.046	0.264	0.210	1.50	T3
22	NSC J0504−4822	570.648	0.310	0.077	0.387	0.249	5.86	L0
23	NSC J0505−4750	1216.806	0.139	0.079	0.218	0.569	1.26	M9
24	NSC J0523−5655	706.547	0.195	0.046	0.241	0.235	1.78	T0
25	NSC J0532−5124	507.731	0.256	0.073	0.329	0.285	5.16	L3
26	NSC J1239−0054	377.062	0.222	0.055	0.277	0.250	4.54	L4
27	NSC J1305−2247	715.907	0.630	0.073	0.703	0.116	9.00	L3
28	NSC J1320−4012	3697.213	0.499	0.073	0.572	0.145	1.38	L1
29	NSC J2023−4844	1093.871	0.290	0.077	0.367	0.267	2.86	L0
30	NSC J2208−5510	430.541	0.206	0.079	0.285	0.384	5.29	M9
31	NSC J2241−4500	418.277	0.297	0.073	0.370	0.244	7.26	L2
32	NSC J2327−5247	6487.802	0.493	0.073	0.566	0.147	0.78	L1
33	NSC J2333−6347	322.740	0.570	0.079	0.649	0.139	19.54	M9
34	NSC J2344+0031	1030.796	0.161	0.073	0.234	0.451	1.60	L2

NOTE— [a]Projected physical separation; [b]Primary mass estimate from either Stassun et al. (2019) or Gentile Fusillo et al. (2021); [c]Secondary mass estimate from either Mamajek (2021) for sources with $M_G < 17$ mag, or from the SpT to dynamical mass values computed in Dupuy & Liu (2017); [d]Total mass (primary mass + secondary mass); [e]Mass ratio (secondary/primary); [f]Binding energy, calculated by multiplying the physical separation by 1.26 to account for inclination angle and eccentricity of the binary orbits (Fischer & Marcy 1992); [g]Spectral type used to derive the secondary's mass.

Table 6. Age, initial and final mass estimates of the white dwarfs

Sys. #	WD type	$T_{\rm eff}$[a] (K)	$\log g$[b]	Mass[c] ($M_\odot$)	MS age[d] (Gyr)	WD age[e] (Gyr)	Tot. age[f] (Gyr)	Init. mass[g] ($M_\odot$)	Final mass[h] ($M_\odot$)
(1)	(2)	(3)	(4)	(5)	(6)	(7)	(8)	(9)	(10)
25	DA	4960 ± 422	7.225 ± 0.507	0.256 ± 0.159	$\cdots$	$2.34^{+2.04}_{-0.91}$	$\cdots$	$\cdots$	$0.33^{+0.21}_{-0.11}$
25	DB	5043 ± 337	7.321 ± 0.393	0.283 ± 0.133	$\cdots$	$2.04^{+1.62}_{-0.65}$	$\cdots$	$\cdots$	$0.32^{+0.16}_{-0.1}$
27	DA	5373 ± 786	8.076 ± 0.670	0.63 ± 0.383	$1.42^{+2.15}_{-1.01}$	$5.25^{+2.27}_{-2.07}$	$7.41^{+1.75}_{-2.06}$	$1.93^{+1.18}_{-0.53}$	$0.65^{+0.12}_{-0.05}$
27	DB	5266 ± 720	8.003 ± 0.632	0.571 ± 0.355	$1.46^{+2.14}_{-1.0}$	$5.39^{+2.22}_{-2.05}$	$7.57^{+1.65}_{-2.01}$	$1.91^{+1.09}_{-0.51}$	$0.65^{+0.1}_{-0.05}$
33	DA	5243 ± 318	8.067 ± 0.282	0.623 ± 0.175	$1.65^{+2.05}_{-0.98}$	$5.52^{+1.84}_{-1.62}$	$7.79^{+1.4}_{-1.59}$	$1.82^{+0.83}_{-0.42}$	$0.64^{+0.07}_{-0.05}$
33	DB	5147 ± 285	8.002 ± 0.253	0.57 ± 0.143	$1.73^{+1.92}_{-0.94}$	$5.73^{+1.7}_{-1.58}$	$8.05^{+1.25}_{-1.5}$	$1.78^{+0.71}_{-0.38}$	$0.63^{+0.06}_{-0.04}$

NOTE— [a,b,c]Effective temperature, surface gravity and mass estimates from Gentile Fusillo et al. (2021); [d]Main sequence age (age of the progenitor star); [e]Cooling age of the white dwarf; [f]Total age (main sequence age + cooling age); [g]Initial mass (mass of the progenitor star); [h]Final mass (mass of the white dwarf).

5. DISCUSSION

Systems #9 and #19 have high tangential velocities of ~ 187 and ~ 158 km s^{-1} respectively, suggesting a possible thick disk or halo membership (Carollo et al. 2010; Dupuy & Liu 2012; Belokurov et al. 2018; Amarante et al. 2020). Further study of these systems is required to determine how old or metal-poor these objects really are.

Systems #13, #14 and #31 have a primary with a high *Gaia* RUWE[3] of ~ 1.9, ~ 14 and ~ 2.7 respectively. A RUWE significantly greater than 1.0 (e.g. >1.4) could indicate that the source is non-single and thus might be an unresolved binary (Belokurov et al. 2020; Penoyre et al. 2020). Given past work suggesting that widely separated ultracool dwarfs from higher mass companions are likely to be found in hierarchical systems, there is an increased probability of finding more hidden companions. (e.g. Burgasser et al. 2003, Faherty et al. 2010, Law et al. 2010). System #31, which is likely a triple system (M+M+L), has already been analyzed in more detail (Kiwy et al. 2021).

Systems #9, #13 and #15 have comoving probabilities well below 100%, when we use a distance constraint in these calculations, indicating that they are likely chance alignments. Systems #9 and #15 also show the largest discrepancies between the primary's parallactic and the secondary's photometric distance (232.5±1.1 pc vs. 121.8±30.2 pc and 258±3.4 pc vs. 128.4±10.7 pc, respectively), implying that these systems (provided the photometric distance is reasonably correct) cannot be physically bound. Whereas system #13 has a much smaller distance difference of only 8.8±14 pc between the primary and the secondary as well as a higher comov-

ing probability (87.0%) compared to systems #9 and #15 (59.8 and 4.5%, respectively), but still well below that of the majority of the systems (> 99%).

6. CONCLUSION

We presented the discovery of 34 new, potential comoving systems found by the means of NSC DR2 and demonstrated that the catalog's proper motions are well suited for the discovery of comoving systems including late-type objects such as brown dwarfs in the L and T regimes. We also showed that the catalog can be used to find close late-type comoving companions to white dwarfs, providing valuable benchmark systems for the difficult task of estimating brown dwarf ages.

According to the literature, none of the 34 identified objects were previously known to have a comoving companion. Some of the systems stand out as having high tangential velocities, suggesting that they could be candidates for low metallicity benchmark systems. The newly discovered systems expand the known sample of benchmark systems involving L and T dwarfs and thus contribute to the further characterization of cool substellar objects.

Spectroscopic follow-up on individual interesting systems is warranted, for instance, to find out how low the metallicity of the high tangential velocity systems actually is, or to clarify the potential binarity of the primaries with a high *Gaia* RUWE value.

[3] Re-normalized Unit Weight Error

REFERENCES

Abbott, T. M. C., Abdalla, F. B., Allam, S., et al. 2018, ApJS, 239, 18, doi: 10.3847/1538-4365/aae9f0

Abbott, T. M. C., Adamów, M., Aguena, M., et al. 2021, ApJS, 255, 20, doi: 10.3847/1538-4365/ac00b3

Amarante, J. A. S., Smith, M. C., & Boeche, C. 2020, MNRAS, 492, 3816, doi: 10.1093/mnras/staa077

Basri, G., & Martín, E. L. 1999, AJ, 118, 2460, doi: 10.1086/301079

Bédard, A., Bergeron, P., Brassard, P., & Fontaine, G. 2020, ApJ, 901, 93, doi: 10.3847/1538-4357/abafbe

Belokurov, V., Erkal, D., Evans, N. W., Koposov, S. E., & Deason, A. J. 2018, MNRAS, 478, 611, doi: 10.1093/mnras/sty982

Belokurov, V., Penoyre, Z., Oh, S., et al. 2020, MNRAS, 496, 1922, doi: 10.1093/mnras/staa1522

Best, W. M. J., Dupuy, T. J., Liu, M. C., Siverd, R. J., & Zhang, Z. 2020, The UltracoolSheet: Photometry, Astrometry, Spectroscopy, and Multiplicity for 3000+ Ultracool Dwarfs and Imaged Exoplanets, doi: 10.5281/zenodo.4169085

Best, W. M. J., Liu, M. C., Magnier, E. A., & Dupuy, T. J. 2021, AJ, 161, 42, doi: 10.3847/1538-3881/abc893

Best, W. M. J., Magnier, E. A., Liu, M. C., et al. 2018, ApJS, 234, 1, doi: 10.3847/1538-4365/aa9982

Bochanski, J. J., West, A. A., Hawley, S. L., & Covey, K. R. 2007, AJ, 133, 531, doi: 10.1086/510240

Burgasser, A. J., Kirkpatrick, J. D., Cruz, K. L., et al. 2006, ApJS, 166, 585, doi: 10.1086/506327

Burgasser, A. J., Kirkpatrick, J. D., Reid, I. N., et al. 2003, ApJ, 586, 512, doi: 10.1086/346263

Burgasser, A. J., McElwain, M. W., Kirkpatrick, J. D., et al. 2004, AJ, 127, 2856, doi: 10.1086/383549

Calissendorff, P., Janson, M., Asensio-Torres, R., & Köhler, R. 2019, A&A, 627, A167, doi: 10.1051/0004-6361/201935319

Carnero Rosell, A., Santiago, B., dal Ponte, M., et al. 2019, MNRAS, 489, 5301, doi: 10.1093/mnras/stz2398

Carollo, D., Beers, T. C., Chiba, M., et al. 2010, ApJ, 712, 692, doi: 10.1088/0004-637X/712/1/692

Choi, J., Dotter, A., Conroy, C., et al. 2016, ApJ, 823, 102, doi: 10.3847/0004-637X/823/2/102

Close, L. M., Siegler, N., Freed, M., & Biller, B. 2003, ApJ, 587, 407, doi: 10.1086/368177

Cummings, J. D., Kalirai, J. S., Tremblay, P. E., Ramirez-Ruiz, E., & Choi, J. 2018, ApJ, 866, 21, doi: 10.3847/1538-4357/aadfd6

Cushing, M. C., Vacca, W. D., & Rayner, J. T. 2004, PASP, 116, 362, doi: 10.1086/382907

Delfosse, X., Beuzit, J. L., Marchal, L., et al. 2004, in Astronomical Society of the Pacific Conference Series, Vol. 318, Spectroscopically and Spatially Resolving the Components of the Close Binary Stars, ed. R. W. Hilditch, H. Hensberge, & K. Pavlovski, 166–174

Dey, A., Schlegel, D. J., Lang, D., et al. 2019, AJ, 157, 168, doi: 10.3847/1538-3881/ab089d

Dotter, A. 2016, ApJS, 222, 8, doi: 10.3847/0067-0049/222/1/8

Dupuy, T. J., & Kraus, A. L. 2013, Science, 341, 1492, doi: 10.1126/science.1241917

Dupuy, T. J., & Liu, M. C. 2012, ApJS, 201, 19, doi: 10.1088/0067-0049/201/2/19

—. 2017, ApJS, 231, 15, doi: 10.3847/1538-4365/aa5e4c

Duquennoy, A., & Mayor, M. 1991, A&A, 500, 337

Eggen, O. J. 1976a, ApJS, 30, 351, doi: 10.1086/190366

—. 1976b, ApJ, 204, 101, doi: 10.1086/154154

Faherty, J. K., Burgasser, A. J., West, A. A., et al. 2010, AJ, 139, 176, doi: 10.1088/0004-6256/139/1/176

Faherty, J. K., Goodman, S., Caselden, D., et al. 2020, ApJ, 889, 176, doi: 10.3847/1538-4357/ab5303

Faherty, J. K., Gagné, J., Popinchalk, M., et al. 2021, ApJ, 923, 48, doi: 10.3847/1538-4357/ac2499

Fischer, D. A., & Marcy, G. W. 1992, ApJ, 396, 178, doi: 10.1086/171708

Fontanive, C., Biller, B., Bonavita, M., & Allers, K. 2018, MNRAS, 479, 2702, doi: 10.1093/mnras/sty1682

Gagné, J., Faherty, J. K., Schneider, A. C., & Meisner, A. M. 2021, CoMover: Bayesian probability of co-moving stars. http://ascl.net/2106.007

Gelino, C. R., Kirkpatrick, J. D., Cushing, M. C., et al. 2011, AJ, 142, 57, doi: 10.1088/0004-6256/142/2/57

Gentile Fusillo, N. P., Tremblay, P. E., Cukanovaite, E., et al. 2021, MNRAS, 508, 3877, doi: 10.1093/mnras/stab2672

Goodwin, S. P., & Whitworth, A. 2007, A&A, 466, 943, doi: 10.1051/0004-6361:20066745

Hartman, Z. D., & Lépine, S. 2020, ApJS, 247, 66, doi: 10.3847/1538-4365/ab79a6

Huélamo, N., Ivanov, V. D., Kurtev, R., et al. 2015, A&A, 578, A1, doi: 10.1051/0004-6361/201525634

Gaia Collaboration, Prusti, T., de Bruijne, J. H. J., et al. 2016, A&A, 595, A1, doi: 10.1051/0004-6361/201629272

Gaia Collaboration, Brown, A. G. A., Vallenari, A., et al. 2018, A&A, 616, A1, doi: 10.1051/0004-6361/201833051

—. 2021, A&A, 649, A1, doi: 10.1051/0004-6361/202039657

Janson, M., Bergfors, C., Brandner, W., et al. 2014, ApJ, 789, 102, doi: 10.1088/0004-637X/789/2/102

Kiman, R., Schmidt, S. J., Angus, R., et al. 2019, AJ, 157, 231, doi: 10.3847/1538-3881/ab1753

Kirkpatrick, J. D., Kellogg, K., Schneider, A. C., et al. 2016, ApJS, 224, 36, doi: 10.3847/0067-0049/224/2/36

Kiwy, F. 2022, AstroToolBox: Java toolkit for identifying and classifying astronomical objects. http://ascl.net/2201.002

Kiwy, F., Faherty, J., Meisner, A., et al. 2021, Research Notes of the American Astronomical Society, 5, 196, doi: 10.3847/2515-5172/ac1f9c

Kraus, A. L., & Hillenbrand, L. A. 2012, ApJ, 757, 141, doi: 10.1088/0004-637X/757/2/141

Kuchner, M. J., Faherty, J. K., Schneider, A. C., et al. 2017, ApJL, 841, L19, doi: 10.3847/2041-8213/aa7200

Lam, M. C., Hambly, N. C., Lodieu, N., et al. 2020, MNRAS, 493, 6001, doi: 10.1093/mnras/staa584

Law, N. M., Dhital, S., Kraus, A., Stassun, K. G., & West, A. A. 2010, ApJ, 720, 1727, doi: 10.1088/0004-637X/720/2/1727

Liu, M. C., Dupuy, T. J., & Allers, K. N. 2016, ApJ, 833, 96, doi: 10.3847/1538-4357/833/1/96

Lu, Y. L., Angus, R., Curtis, J. L., David, T. J., & Kiman, R. 2021, AJ, 161, 189, doi: 10.3847/1538-3881/abe4d6

Luyten, W. J. 1995, VizieR Online Data Catalog, I/98A

Mamajek, E. E. 2021, A Modern Mean Dwarf Stellar Color and Effective Temperature Sequence, 2021.03.02. https://www.pas.rochester.edu/~emamajek/ EEM_dwarf_UBVIJHK_colors_Teff.txt

Marocco, F., Eisenhardt, P. R. M., Fowler, J. W., et al. 2021, ApJS, 253, 8, doi: 10.3847/1538-4365/abd805

Martín, E. L., Brandner, W., & Basri, G. 1999, Science, 283, 1718, doi: 10.1126/science.283.5408.1718

Martín, E. L., Basri, G., Brandner, W., et al. 1998, ApJL, 509, L113, doi: 10.1086/311775

Meisner, A. M., Lang, D., & Schlegel, D. J. 2017, AJ, 154, 161, doi: 10.3847/1538-3881/aa894e

—. 2018, AJ, 156, 69, doi: 10.3847/1538-3881/aacbcd

Nidever, D. L., Dey, A., Fasbender, K., et al. 2021, AJ, 161, 192, doi: 10.3847/1538-3881/abd6e1

Ochsenbein, F., Bauer, P., & Marcout, J. 2000, A&AS, 143, 23, doi: 10.1051/aas:2000169

Paxton, B., Bildsten, L., Dotter, A., et al. 2011, ApJS, 192, 3, doi: 10.1088/0067-0049/192/1/3

Paxton, B., Cantiello, M., Arras, P., et al. 2013, ApJS, 208, 4, doi: 10.1088/0067-0049/208/1/4

Paxton, B., Marchant, P., Schwab, J., et al. 2015, ApJS, 220, 15, doi: 10.1088/0067-0049/220/1/15

Penoyre, Z., Belokurov, V., Wyn Evans, N., Everall, A., & Koposov, S. E. 2020, MNRAS, 495, 321, doi: 10.1093/mnras/staa1148

Pokorny, R. S., Jones, H. R. A., & Hambly, N. C. 2003, A&A, 397, 575, doi: 10.1051/0004-6361:20021385

Raghavan, D., McAlister, H. A., Henry, T. J., et al. 2010, ApJS, 190, 1, doi: 10.1088/0067-0049/190/1/1

Reylé, C. 2018, A&A, 619, L8, doi: 10.1051/0004-6361/201834082

Salim, S., & Gould, A. 2003, ApJ, 582, 1011, doi: 10.1086/344822

Skrzypek, N., Warren, S. J., & Faherty, J. K. 2016, A&A, 589, A49, doi: 10.1051/0004-6361/201527359

Smart, R. L., Marocco, F., Sarro, L. M., et al. 2019, MNRAS, 485, 4423, doi: 10.1093/mnras/stz678

Stassun, K. G., Oelkers, R. J., Paegert, M., et al. 2019, AJ, 158, 138, doi: 10.3847/1538-3881/ab3467

Sutherland, W., Emerson, J., Dalton, G., et al. 2015, A&A, 575, A25, doi: 10.1051/0004-6361/201424973

Vacca, W. D., Cushing, M. C., & Rayner, J. T. 2003, PASP, 115, 389, doi: 10.1086/346193

Wenger, M., Ochsenbein, F., Egret, D., et al. 2000, A&AS, 143, 9, doi: 10.1051/aas:2000332

Winters, J. G., Henry, T. J., Jao, W.-C., et al. 2019, AJ, 157, 216, doi: 10.3847/1538-3881/ab05dc

Wright, E. L., Eisenhardt, P. R. M., Mainzer, A. K., et al. 2010, AJ, 140, 1868, doi: 10.1088/0004-6256/140/6/1868

Wroblewski, H., & Torres, C. 1996, A&AS, 115, 481

APPENDIX

Table 7. Optical and infrared photometry

Sys. #	C.ª	G_{BP} / J_{2M} (mag)	G / H_{2M} (mag)	G_{RP} / Ks_{2M} (mag)	r_{PS1} / J_{VHS} (mag)	i_{PS1} / H_{VHS} (mag)	z_{PS1} / Ks_{VHS} (mag)	y_{PS1} / $W1_A$ (mag)	r_{NSC} / $W2_A$ (mag)	i_{NSC} / $W3_A$ (mag)	z_{NSC} / $W1_C$ (mag)	Y_{NSC} / $W2_C$ (mag)
1	A	20.314±0.065	17.904±0.003	16.491±0.005	19.221±0.008	17.174±0.004	16.203±0.003	15.702±0.004	19.031±0.003	16.947±0.002	16.005±0.001	15.643±0.002
		14.301±0.029	13.688±0.04	13.381±0.034	···	···	···	13.208±0.025	12.995±0.03	>12.226	13.2±0.013	12.995±0.011
	B	···	···	···	22.159±0.343	21.797±0.183	20.609±0.129	19.641±0.052	···	21.821±0.033	20.288±0.015	19.696±0.03
		···	···	···	···	···	···	15.278±0.039	15.137±0.1	>12.551	15.373±0.021	15.138±0.031
2	A	20.79±0.103	17.983±0.003	16.495±0.006	19.822±0.015	17.256±0.005	16.147±0.003	15.566±0.004	19.519±0.004	16.944±0.002	15.879±0.001	15.528±0.002
		14.118±0.03	13.576±0.029	13.307±0.033	···	···	···	13.004±0.025	12.788±0.026	>12.514	···	···
	B	···	···	···	···	···	···	···	···	···	21.238±0.033	20.145±0.044
		···	···	···	···	···	···	···	···	···	17.575±0.075	15.91±0.057
3	A	21.476±0.216	20.34±0.006	19.048±0.045	21.698±0.041	19.564±0.015	18.613±0.018	18.174±0.018	21.477±0.014	19.415±0.003	18.484±0.002	18.128±0.011
		16.766±0.144	>15.939	>15.37	···	···	···	15.465±0.043	15.231±0.104	>12.139	15.824±0.081	15.684±0.098
	B	···	···	···	···	20.648±0.018	19.405±0.035	18.863±0.02	22.883±0.045	20.408±0.005	19.229±0.004	18.827±0.019
		···	···	···	···	···	···	···	···	···	16.479±0.037	16.281±0.085
4	A	18.001±0.011	16.487±0.003	15.289±0.004	17.13±0.002	15.771±0.006	15.168±0.005	14.853±0.006	17.021±0.001	···	15.059±0.001	14.796±0.001
		13.599±0.026	12.968±0.023	12.804±0.027	···	···	···	12.585±0.024	12.47±0.024	12.619±0.526	12.66±0.014	12.511±0.013
	B	21.562±0.183	21.128±0.021	19.481±0.167	···	20.572±0.036	19.169±0.017	18.328±0.019	22.863±0.045	20.189±0.005	18.781±0.002	18.203±0.005
		16.586±0.114	15.862±0.181	>14.405	···	···	···	···	···	···	15.245±0.049	15.234±0.052
5	A	14.78±0.003	13.697±0.003	12.662±0.004	13.958±0.003	13.104±0.022	12.712±···	12.475±0.001	···	···	···	···
		11.348±0.021	10.753±0.022	10.535±0.021	···	···	···	10.395±0.023	10.307±0.019	10.185±0.064	10.414±0.012	10.312±0.008
	B	21.549±0.261	20.745±0.01	19.128±0.048	···	···	18.614±0.05	17.557±0.042	23.131±0.042	19.676±0.006	18.18±0.004	17.674±0.007
		15.996±0.12	15.418±0.269	14.854±0.137	···	···	···	···	···	···	···	···
6	A	16.744±0.005	15.396±0.003	14.252±0.004	15.908±0.002	14.717±0.002	14.183±0.003	13.926±0.004	15.81±0.003	14.629±0.003	14.086±0.002	13.859±0.002
		12.88±0.03	12.178±0.035	11.902±0.029	···	···	···	11.669±0.023	11.595±0.022	11.477±0.193	11.633±0.011	11.591±0.008
	B	···	···	···	···	20.815±0.053	19.479±0.016	18.618±0.027	22.797±0.166	20.541±0.014	19.098±0.007	18.546±0.023
		17.153±0.235	16.388±0.248	15.454±0.205	···	···	···	···	···	···	15.351±0.039	15.312±0.051
7	A	18.023±0.008	16.489±0.003	15.281±0.004	17.19±0.004	15.782±0.002	15.157±0.002	14.857±0.002	17.034±0.002	15.661±0.002	15.06±0.001	14.811±0.001
		13.679±0.03	13.141±0.031	12.905±0.031	13.598±0.002	13.154±0.002	12.892±0.003	12.732±0.023	12.504±0.024	12.237±0.413	12.707±0.014	12.524±0.01
	B	···	···	···	···	···	21.095±0.139	19.593±0.134	···	22.865±0.095	21.032±0.039	20.29±0.071
		···	···	···	18.359±0.046	17.933±0.066	17.176±0.085	16.213±0.062	16.274±0.217	12.404±0.454	16.656±0.043	16.998±0.168
8	A	15.326±0.004	14.455±0.003	13.532±0.004	14.554±0.004	13.931±0.002	13.653±0.003	13.486±0.001	14.513±0.002	···	···	13.413±0.002
		12.378±0.023	11.739±0.022	11.545±0.019	12.467±0.001	12.007±0.001	11.63±0.001	11.466±0.023	11.434±0.022	11.601±0.186	11.483±0.013	11.443±0.009
	B	···	···	···	···	···	···	···	···	21.001±0.01	19.302±0.006	18.486±0.011
		···	···	···	17.181±0.012	16.635±0.015	16.322±0.025	···	···	···	···	···
9	A	15.105±0.003	14.36±0.003	13.514±0.004	14.388±0.001	13.903±0.002	13.689±0.004	13.559±0.002	···	···	···	13.502±0.001
		12.467±0.024	11.813±0.022	11.661±0.021	12.484±0.001	···	11.672±0.001	11.632±0.023	11.633±0.022	11.344±0.151	11.618±0.012	11.629±0.009
	B	···	···	···	···	···	21.343±0.197	20.17±0.144	···	22.896±0.056	21.084±0.029	20.623±0.057
		···	···	···	18.781±0.053	···	17.728±0.121	17.589±0.168	16.659±0.274	>12.722	17.405±0.071	16.842±0.131

Table 7 continued

Table 7 *(continued)*

Sys. #	C.ᵃ	G_{BP} / J_{2M} (mag)	G / H_{2M} (mag)	G_{RP} / Ks_{2M} (mag)	r_{PS1} / J_{VHS} (mag)	i_{PS1} / H_{VHS} (mag)	z_{PS1} / Ks_{VHS} (mag)	y_{PS1} / $W1_A$ (mag)	r_{NSC} / $W2_A$ (mag)	i_{NSC} / $W3_A$ (mag)	z_{NSC} / $W1_C$ (mag)	Y_{NSC} / $W2_C$ (mag)
10	A	14.843±0.003	13.666±0.003	12.587±0.004	⋯	⋯	⋯	⋯	⋯	⋯	⋯	12.344±0.002
		11.212±0.022	10.607±0.027	10.384±0.021	12.176±0.001	12.859±0.002	11.559±0.001	10.218±0.023	10.114±0.02	9.924±0.049	10.235±0.012	10.128±0.008
	B	⋯	⋯	⋯	⋯	⋯	⋯	⋯	⋯	22.485±0.049	20.613±0.022	20.126±0.048
		⋯	⋯	⋯	17.928±0.045	17.092±0.039	16.499±0.044	15.677±0.042	15.302±0.077	>12.542	15.754±0.02	15.538±0.037
11	A	21.161±0.244	20.374±0.007	18.853±0.043	18.805± ⋯	19.7±0.009	18.519±0.016	17.877±0.011	22.205±0.018	19.411±0.005	18.27±0.003	17.859±0.013
		16.219±0.095	15.645±0.114	15.432±0.16	⋯	⋯	⋯	15.312±0.038	15.079±0.077	>12.66	15.293±0.02	15.116±0.033
	B	⋯	⋯	⋯	⋯	⋯	⋯	⋯	⋯	⋯	22.094±0.062	⋯
		⋯	⋯	⋯	⋯	⋯	⋯	⋯	⋯	⋯	17.519±0.092	16.971±0.163
12	A	20.823±0.146	19.099±0.004	17.703±0.014	⋯	⋯	⋯	⋯	20.01±0.005	18.048±0.002	17.203±0.002	16.944±0.003
		15.693±0.062	15.243±0.098	14.685±0.122	15.575±0.005	⋯	14.766±0.01	14.564±0.028	14.355±0.036	>12.835	14.516±0.014	14.346±0.014
	B	⋯	⋯	⋯	⋯	⋯	⋯	⋯	⋯	22.347±0.04	20.848±0.022	20.367±0.044
		⋯	⋯	⋯	18.494±0.051	⋯	17.375±0.092	17.014±0.079	16.698±0.202	>12.674	16.898±0.034	16.678±0.082
13	A	16.142±0.005	14.725±0.003	13.551±0.004	⋯	⋯	⋯	⋯	15.151±0.001	⋯	⋯	13.137±0.002
		11.964±0.026	11.372±0.025	11.108±0.021	11.949±0.001	⋯	11.188±0.001	10.943±0.022	10.783±0.02	10.653±0.081	10.884±0.01	10.777±0.007
	B	21.516±0.188	20.975±0.012	19.365±0.117	⋯	⋯	⋯	⋯	22.223±0.045	19.867±0.005	18.313±0.004	17.432±0.007
		16.127±0.112	15.417±0.128	15.01±0.121	16.149±0.006	⋯	15.066±0.01	⋯	⋯	⋯	15.037±0.036	14.63±0.034
14	A	19.859±0.064	17.536±0.007	16.044±0.008	18.838±0.003	16.711±0.003	15.765±0.003	15.281±0.005	18.63±0.002	16.509±0.001	15.582±0.001	15.225±0.001
		13.914±0.03	13.352±0.029	13.013±0.033	13.824±0.002	13.332±0.002	13.004±0.003	12.778±0.023	12.547±0.025	11.877±0.203	12.788±0.011	12.56±0.01
	B	⋯	⋯	⋯	⋯	⋯	20.784±0.202	19.466±0.176	⋯	22.787±0.091	20.742±0.026	20.023±0.055
		⋯	⋯	⋯	18.07±0.036	17.403±0.04	16.787±0.048	⋯	⋯	⋯	16.173±0.052	15.958±0.077
15	A	17.371±0.01	16.332±0.003	15.325±0.005	16.543±0.002	15.737±0.003	15.363±0.002	15.162±0.005	16.507±0.002	15.698±0.001	15.331±0.001	15.14±0.001
		14.024±0.028	13.47±0.03	13.312±0.034	⋯	⋯	⋯	13.152±0.023	13.007±0.029	>12.254	13.15±0.013	13.04±0.011
	B	⋯	⋯	⋯	⋯	⋯	⋯	⋯	⋯	21.527±0.038	20.078±0.016	19.657±0.04
		⋯	⋯	⋯	⋯	⋯	⋯	⋯	⋯	⋯	⋯	⋯
16	A	16.233±0.005	15.141±0.003	14.099±0.004	15.432±0.002	14.525±0.003	14.098±0.004	13.89±0.003	15.37±0.002	⋯	14.039±0.002	13.857±0.001
		12.749±0.022	12.196±0.026	12.031±0.023	12.73±0.001	⋯	11.981±0.002	11.871±0.023	11.729±0.021	11.679±0.164	11.799±0.011	11.73±0.009
	B	19.444±1.812	20.911±0.018	19.237±0.079	⋯	20.172±0.024	18.907±0.017	18.202±0.008	22.37±0.061	19.876±0.007	18.631±0.005	18.158±0.011
		16.651±0.178	>14.644	>14.182	16.737±0.01	⋯	15.97±0.035	⋯	⋯	⋯	⋯	⋯
17	A	17.794±0.012	16.382±0.003	15.226±0.005	16.938±0.002	15.691±0.002	15.13±0.003	14.856±0.006	16.842±0.002	15.58±0.001	15.051±0.001	14.82±0.001
		13.705±0.029	13.156±0.03	12.956±0.033	13.615±0.002	⋯	12.915±0.002	12.764±0.024	12.545±0.023	12.255±0.256	12.809±0.016	12.6±0.012
	B	⋯	⋯	⋯	⋯	21.261±0.037	19.878±0.02	18.913±0.042	⋯	20.983±0.021	19.419±0.009	18.654±0.021
		⋯	⋯	⋯	17.137±0.013	⋯	16.283±0.032	⋯	⋯	⋯	15.58±0.042	15.292±0.05
18	A	21.215±0.1	19.343±0.003	17.989±0.013	20.681±0.039	18.589±0.007	17.692±0.005	17.28±0.013	20.474±0.007	18.383±0.003	17.548±0.002	17.238±0.005
		16.007±0.087	15.324±0.097	15.199±0.181	15.902±0.005	⋯	15.174±0.011	14.816±0.03	14.453±0.044	>12.711	14.793±0.02	14.578±0.024
	B	⋯	⋯	⋯	⋯	21.338±0.179	⋯	19.292±0.016	⋯	21.485±0.022	19.79±0.01	19.252±0.024
		⋯	⋯	⋯	17.504±0.016	⋯	16.703±0.041	⋯	⋯	⋯	16.845±0.051	16.738±0.13

Table 7 continued

Table 7 *(continued)*

Sys. #	C.[a]	G_{BP} / J_{2M}	G / H_{2M}	G_{RP} / Ks_{2M}	r_{PS1} / J_{VHS}	i_{PS1} / H_{VHS}	z_{PS1} / Ks_{VHS}	y_{PS1} / $W1_A$	r_{NSC} / $W2_A$	i_{NSC} / $W3_A$	z_{NSC} / $W1_C$	Y_{NSC} / $W2_C$
		(mag)	(mag)	(mag)	(mag)	(mag)	(mag)	(mag)	(mag)	(mag)	(mag)	(mag)
19	A	17.12±0.005	15.791±0.003	14.653±0.004	16.315±0.004	15.112±0.002	14.544±0.003	14.309±0.002	16.219±0.002	15.016±0.004	14.508±0.002	14.266±0.002
		13.206±0.029	12.655±0.029	12.478±0.027	13.137±0.001	···	12.484±0.002	12.244±0.062	12.065±0.022	11.976±0.262	12.256±0.012	12.094±0.009
	B	···	···	···	···	20.845±0.036	19.303±0.027	18.401±0.064	23.34±0.077	20.535±0.012	18.984±0.006	18.446±0.018
		16.631±0.148	15.883±0.195	>15.028	16.794±0.009	···	15.972±0.024	···	···	···	15.509±0.031	15.043±0.037
20	A	17.208±0.005	15.813±0.003	14.656±0.004	···	···	···	···	16.209±0.002	···	···	14.288±0.001
		13.096±0.026	12.533±0.022	12.287±0.023	13.081±0.001	···	12.333±0.002	12.139±0.214	11.941±0.022	11.873±0.204	12.15±0.013	11.987±0.009
	B	···	···	···	···	···	···	···	···	22.723±0.064	20.934±0.034	20.393±0.059
		···	···	···	18.268±0.033	···	17.08±0.062	16.12±0.524	16.166±0.145	>12.897	16.353±0.028	16.209±0.064
21	A	16.38±0.004	14.902±0.003	13.718±0.004	15.493±0.004	14.204±0.004	13.622±0.004	13.33±0.003	15.383±0.002	14.047±0.003	13.504±0.002	13.242±0.002
		12.138±0.023	11.6±0.028	11.299±0.025	12.072±0.001	···	11.295±0.001	11.125±0.023	10.947±0.02	10.866±0.081	11.125±0.012	10.957±0.009
	B	···	···	···	···	···	···	19.657±0.159	···	···	20.563±0.017	19.641±0.027
		···	···	···	17.482±0.016	···	16.864±0.053	···	···	···	16.121±0.028	15.247±0.031
22	A	16.287±0.004	14.888±0.003	13.728±0.004	···	···	···	···	15.306±0.003	···	···	13.343±0.001
		12.177±0.023	11.643±0.022	11.343±0.019	12.44±0.001	···	11.646±0.001	11.205±0.023	11.041±0.021	11.02±0.079	11.142±0.01	11.032±0.008
	B	···	···	···	···	···	···	···	22.87±0.074	20.439±0.012	18.955±0.008	18.089±0.014
		16.516±0.145	15.77±0.147	15.314±0.157	16.466±0.007	···	15.4±0.015	···	···	···	15.098±0.027	14.808±0.028
23	A	20.287±0.111	18.405±0.003	17.092±0.011	···	···	···	···	19.248±0.003	17.446±0.001	16.676±0.001	16.447±0.002
		15.219±0.049	14.59±0.057	14.487±0.081	15.071±0.003	···	14.335±0.006	14.156±0.025	13.924±0.033	>13.003	14.182±0.014	13.977±0.012
	B	···	···	···	···	···	···	···	23.424±0.06	20.455±0.005	19.041±0.005	18.622±0.011
		17.193±0.217	16.583±0.261	15.615±0.218	16.911±0.011	···	15.984±0.025	···	···	···	15.813±0.02	15.587±0.031
24	A	17.021±0.006	15.334±0.003	14.091±0.004	···	···	···	···	15.968±···	···	···	13.566±0.001
		12.333±0.023	11.782±0.024	11.501±0.025	12.295±0.001	···	11.543±0.001	11.336±0.024	11.142±0.02	11.047±0.082	11.297±0.01	11.141±0.008
	B	···	···	···	···	···	···	···	···	···	21.09±0.026	20.484±0.066
		···	···	···	18.318±0.037	···	16.782±0.054	···	···	···	15.818±0.021	15.46±0.03
25	A	20.505±0.077	20.017±0.006	19.405±0.08	···	···	···	···	20.044±0.005	19.879±0.007	19.876±0.012	19.952±0.042
		···	···	···	19.009±0.052	18.695±0.088	18.521±0.196	···	···	···	···	···
	B	···	···	···	···	···	···	···	···	23.344±0.189	21.694±0.047	20.859±0.12
		···	···	···	18.922±0.049	18.206±0.057	17.432±0.073	···	···	···	16.892±0.031	16.485±0.062
26	A	16.154±0.005	14.517±0.003	13.285±0.004	15.275±0.003	13.79±0.002	13.132±0.001	12.832±0.003	15.107±0.001	13.636±0.001	13.027±0.003	12.738±0.002
		11.588±0.023	10.978±0.024	10.704±0.021	···	···	···	10.549±0.022	10.379±0.02	10.225±0.079	10.428±0.01	10.335±0.007
	B	···	···	···	···	21.172±0.05	19.602±0.025	18.586±0.018	22.875±0.173	20.639±0.029	19.118±0.007	18.468±0.041
		16.563±0.147	15.566±0.113	14.754±0.127	···	···	···	14.074±0.138	13.963±0.141	>12.058	14.272±0.02	14.077±0.02
27	A	20.964±0.155	20.459±0.008	19.939±0.115	20.366±0.027	20.154±0.023	20.021±0.03	19.827±0.07	20.476±0.006	20.241±0.005	20.151±0.008	20.004±0.016
		···	···	···	19.203±0.144	···	···	···	···	···	···	···
	B	···	···	···	···	21.451±0.053	20.208±0.035	19.195±0.028	···	21.279±0.013	19.732±0.006	19.117±0.008
		···	···	···	17.379±0.028	···	16.329±0.053	15.862±0.049	15.51±0.109	>12.796	15.929±0.026	15.623±0.048

Table 7 *continued*

Table 7 *(continued)*

Sys. #	C.ª	G_{BP} / J_{2M} (mag)	G / H_{2M} (mag)	G_{RP} / Ks_{2M} (mag)	r_{PS1} / J_{VHS} (mag)	i_{PS1} / H_{VHS} (mag)	z_{PS1} / Ks_{VHS} (mag)	y_{PS1} / $W1_A$ (mag)	r_{NSC} / $W2_A$ (mag)	i_{NSC} / $W3_A$ (mag)	z_{NSC} / $W1_C$ (mag)	Y_{NSC} / $W2_C$ (mag)
28	A	14.234±0.003	13.083±0.003	12.017±0.004	⋯	⋯	⋯	⋯	13.328±0.008	⋯	⋯	⋯
		10.633±0.026	10±0.026	9.768±0.021	11.202±0.001	⋯	10.49±0.001	9.639±0.022	9.576±0.021	9.406±0.036	9.645±0.013	9.586±0.009
	B	⋯	⋯	⋯	⋯	⋯	⋯	⋯	22.795±0.033	20.189±0.007	18.7±0.003	18.196±0.011
		16.322±0.105	15.412±0.092	15.023±0.128	16.137±0.013	⋯	14.9±0.016	14.516±0.03	14.387±0.045	>12.574	14.493±0.017	14.324±0.019
29	A	17.269±0.008	15.645±0.003	14.418±0.004	⋯	⋯	⋯	⋯	16.264±0.001	⋯	⋯	13.914±0.003
		12.657±0.024	12.162±0.022	11.889±0.027	12.646±0.001	12.221±0.001	11.929±0.001	11.708±0.022	11.568±0.021	11.594±0.224	⋯	⋯
	B	⋯	⋯	⋯	⋯	⋯	⋯	⋯	23.413±0.068	20.94±0.018	19.395±0.01	18.86±0.03
		⋯	⋯	⋯	16.939±0.018	16.211±0.02	15.764±0.021	16.226±0.056	15.824±0.137	>12.081	15.364±0.021	15.579±0.055
30	A	18.678±0.019	16.716±0.003	15.398±0.004	⋯	⋯	⋯	⋯	17.533±0.001	15.777±0.001	14.98±0.001	14.729±0.001
		13.465±0.029	12.875±0.032	12.584±0.037	13.341±0.001	12.85±0.002	12.544±0.002	12.262±0.023	12.083±0.023	11.634±0.249	12.223±0.01	12.081±0.008
	B	⋯	⋯	⋯	⋯	⋯	⋯	⋯	22.81±0.056	20.423±0.013	18.995±0.008	18.395±0.014
		⋯	⋯	⋯	16.61±0.012	15.971±0.014	15.472±0.015	⋯	⋯	⋯	⋯	⋯
31	A	17.61±0.007	15.668±0.004	14.245±0.004	⋯	⋯	⋯	⋯	16.452±0.001	⋯	13.795±0.001	13.516±0.001
		16.168±0.105	15.371±0.126	14.611±0.084	12.267±0.001	⋯	11.417±0.001	11.103±0.025	10.928±0.023	10.827±0.102	11.136±0.014	10.967±0.01
	B	⋯	21.101±0.023	19.38±0.089	⋯	⋯	⋯	⋯	22.336±0.036	20.117±0.008	18.684±0.005	18.154±0.014
		⋯	⋯	⋯	16.136±0.006	⋯	14.761±0.008	13.993±0.135	13.714±0.134	>12.362	14.622±0.027	14.554±0.031
32	A	15.375±0.003	14.247±0.003	13.181±0.004	⋯	⋯	⋯	⋯	14.501±0.003	13.513±0.003	13.064±0.001	12.919±0.001
		11.815±0.024	11.169±0.022	10.964±0.023	12.205±0.001	11.801±0.001	11.357±0.001	10.814±0.023	10.755±0.021	10.534±0.085	10.836±0.011	10.75±0.008
	B	⋯	⋯	⋯	⋯	⋯	⋯	⋯	23.633±0.106	21.98±0.013	20.483±0.004	19.949±0.025
		⋯	⋯	⋯	17.81±0.022	17.08±0.026	16.449±0.031	16.197±0.05	15.895±0.109	>12.271	16.146±0.026	15.779±0.043
33	A	20.477±0.057	19.994±0.005	19.467±0.053	⋯	⋯	⋯	⋯	19.968±0.005	19.775±0.007	19.656±0.01	19.62±0.029
		⋯	⋯	⋯	18.616±0.055	⋯	18.372±0.249	⋯	⋯	⋯	⋯	⋯
	B	⋯	⋯	⋯	⋯	⋯	⋯	⋯	23.359±0.155	21.013±0.017	19.483±0.009	18.977±0.016
		⋯	⋯	⋯	17.125±0.015	⋯	16.009±0.029	15.752±0.043	15.268±0.079	>12.223	15.6±0.019	15.348±0.031
34	A	20.057±0.088	18.006±0.003	16.641±0.008	19.131±0.006	17.269±0.002	16.396±0.003	15.931±0.004	18.929±0.003	17.147±0.001	16.219±0.001	15.878±0.002
		14.557±0.031	14.051±0.051	13.637±0.032	14.523±0.003	14.033±0.004	13.713±0.004	13.432±0.025	13.219±0.035	>11.68	13.494±0.013	13.313±0.012
	B	⋯	⋯	⋯	⋯	21.832±0.087	20.714±0.061	19.823±0.035	⋯	21.883±0.029	20.379±0.016	19.754±0.044
		⋯	⋯	⋯	17.639±0.039	16.856±0.042	16.168±0.031	⋯	⋯	⋯	15.607±0.024	15.331±0.043

NOTE— [a] Component, where A is the primary and B the secondary of the system.
Gaia photometry is from EDR3, Pan-STARRS and NSC photometry is from DR2, VHS photometry is from DR5.
The photometric band subscripts *2M*, *A* and *C* stand for 2MASS, AllWISE and CatWISE, respectively.

Table 8. Mean photometric uncertainties per band and color

| Catalog | Band | Primary photometric uncertainties | | | | | Secondary photometric uncertainties | | | | |
| | | Number | **Mean** | Min | Median | Max | Number | **Mean** | Min | Median | Max |
	Color	of objects	**(mag)**	(mag)	(mag)	(mag)	of objects	**(mag)**	(mag)	(mag)	(mag)
Gaia EDR3	BP	34	**0.046**	0.003	0.009	0.244	...	...	...	...	
Gaia EDR3	G	34	**0.004**	0.003	0.003	0.008	5	**0.017**	0.010	0.018	0.023
Gaia EDR3	RP	34	**0.014**	0.004	0.004	0.115	5	**0.100**	0.048	0.089	0.167
SDSS DR16	g	10	**0.050**	0.003	0.017	0.378	...	...	...	...	
SDSS DR16	r	10	**0.019**	0.003	0.010	0.119	...	...	...	...	
SDSS DR16	i	10	**0.006**	0.001	0.005	0.021	5	**0.156**	0.051	0.150	0.330
SDSS DR16	z	10	**0.007**	0.003	0.005	0.024	5	**0.114**	0.064	0.101	0.198
PS1 DR2	g	18	**0.012**	0.001	0.007	0.047	...	...	...	...	
PS1 DR2	r	19	**0.009**	0.001	0.004	0.041	1	**0.343**	0.343	0.343	0.343
PS1 DR2	i	20	**0.006**	0.002	0.004	0.023	11	**0.069**	0.018	0.050	0.183
PS1 DR2	z	19	**0.006**	0.001	0.003	0.030	14	**0.069**	0.016	0.043	0.202
PS1 DR2	y	20	**0.008**	0.001	0.004	0.070	16	**0.061**	0.008	0.042	0.176
NSC DR2	g	33	**0.009**	0.001	0.003	0.093	...	...	...	...	
NSC DR2	r	30	**0.004**	0.001	0.003	0.018	16	**0.078**	0.033	0.065	0.173
NSC DR2	i	21	**0.003**	0.001	0.002	0.007	30	**0.031**	0.005	0.018	0.189
NSC DR2	z	24	**0.003**	0.001	0.002	0.012	34	**0.015**	0.002	0.009	0.062
NSC DR2	y	32	**0.005**	0.001	0.002	0.042	33	**0.031**	0.005	0.024	0.120
DES DR1	g	30	**0.014**	0.000	0.001	0.204	...	...	...	...	
DES DR1	r	30	**0.005**	0.000	0.001	0.053	29	**0.374**	0.020	0.148	2.487
DES DR1	i	30	**0.003**	0.000	0.003	0.009	29	**0.115**	0.010	0.024	1.571
DES DR1	z	30	**0.004**	0.000	0.003	0.015	29	**0.026**	0.004	0.012	0.114
DES DR1	y	30	**0.005**	0.000	0.001	0.054	29	**0.047**	0.007	0.026	0.186
2MASS	J	31	**0.038**	0.021	0.028	0.144	10	**0.152**	0.105	0.147	0.235
2MASS	H	30	**0.040**	0.022	0.029	0.126	9	**0.182**	0.092	0.181	0.269
2MASS	K	30	**0.043**	0.019	0.028	0.181	7	**0.156**	0.121	0.137	0.218
VHS DR5	J	25	**0.012**	0.001	0.001	0.144	25	**0.024**	0.006	0.016	0.053
VHS DR5	H	9	**0.011**	0.001	0.002	0.088	9	**0.035**	0.014	0.039	0.066
VHS DR5	K	24	**0.021**	0.001	0.002	0.249	25	**0.042**	0.008	0.032	0.121
CatWISE2020	W1	29	**0.015**	0.010	0.013	0.081	29	**0.035**	0.017	0.028	0.092
CatWISE2020	W2	29	**0.014**	0.007	0.009	0.098	29	**0.059**	0.019	0.048	0.168
Weighted mean	...	...	**0.015**	...	...	...	...	**0.078**	...	...	
Gaia EDR3	BP-RP	...	**0.048**	...	...	...	...	...	...	...	
Gaia EDR3	G-RP	...	**0.015**	...	...	...	...	**0.101**	...	...	
SDSS DR16	g-r	...	**0.053**	...	...	...	...	...	...	...	
SDSS DR16	r-i	...	**0.019**	...	...	...	...	...	...	...	
SDSS DR16	i-z	...	**0.009**	...	...	...	...	**0.194**	...	...	
PS1 DR2	g-r	...	**0.015**	...	...	...	...	...	...	...	
PS1 DR2	r-i	...	**0.011**	...	...	...	...	**0.350**	...	...	
PS1 DR2	i-z	...	**0.009**	...	...	...	...	**0.098**	...	...	
PS1 DR2	z-y	...	**0.010**	...	...	...	...	**0.093**	...	...	

Table 8 *continued*

Kiwy et al. 2022

Table 8 *(continued)*

Catalog	Band Color	Primary photometric uncertainties					Secondary photometric uncertainties				
		Number of objects	**Mean (mag)**	Min (mag)	Median (mag)	Max (mag)	Number of objects	**Mean (mag)**	Min (mag)	Median (mag)	Max (mag)
NSC DR2	g-r	$\cdots$	**0.010**	$\cdots$	$\cdots$	$\cdots$	$\cdots$	$\cdots$	$\cdots$	$\cdots$	
NSC DR2	r-i	$\cdots$	**0.005**	$\cdots$	$\cdots$	$\cdots$	$\cdots$	**0.084**	$\cdots$	$\cdots$	
NSC DR2	i-z	$\cdots$	**0.004**	$\cdots$	$\cdots$	$\cdots$	$\cdots$	**0.035**	$\cdots$	$\cdots$	
NSC DR2	z-y	$\cdots$	**0.006**	$\cdots$	$\cdots$	$\cdots$	$\cdots$	**0.035**	$\cdots$	$\cdots$	
DES DR1	g-r	$\cdots$	**0.015**	$\cdots$	$\cdots$	$\cdots$	$\cdots$	$\cdots$	$\cdots$	$\cdots$	
DES DR1	r-i	$\cdots$	**0.005**	$\cdots$	$\cdots$	$\cdots$	$\cdots$	**0.391**	$\cdots$	$\cdots$	
DES DR1	i-z	$\cdots$	**0.005**	$\cdots$	$\cdots$	$\cdots$	$\cdots$	**0.118**	$\cdots$	$\cdots$	
DES DR1	z-y	$\cdots$	**0.006**	$\cdots$	$\cdots$	$\cdots$	$\cdots$	**0.053**	$\cdots$	$\cdots$	
2MASS	J-H	$\cdots$	**0.055**	$\cdots$	$\cdots$	$\cdots$	$\cdots$	**0.237**	$\cdots$	$\cdots$	
2MASS	H-K	$\cdots$	**0.058**	$\cdots$	$\cdots$	$\cdots$	$\cdots$	**0.239**	$\cdots$	$\cdots$	
2MASS	J-K	$\cdots$	**0.058**	$\cdots$	$\cdots$	$\cdots$	$\cdots$	**0.218**	$\cdots$	$\cdots$	
VHS DR5	J-H	$\cdots$	**0.016**	$\cdots$	$\cdots$	$\cdots$	$\cdots$	**0.043**	$\cdots$	$\cdots$	
VHS DR5	H-K	$\cdots$	**0.024**	$\cdots$	$\cdots$	$\cdots$	$\cdots$	**0.055**	$\cdots$	$\cdots$	
VHS DR5	J-K	$\cdots$	**0.024**	$\cdots$	$\cdots$	$\cdots$	$\cdots$	**0.048**	$\cdots$	$\cdots$	
CatWISE2020	W1-W2	$\cdots$	**0.021**	$\cdots$	$\cdots$	$\cdots$	$\cdots$	**0.069**	$\cdots$	$\cdots$	

Note— The mean uncertainties of the colors correspond to the propagated mean uncertainties in the respective bands.